# ENSO Asymmetry in CMIP5 Models

Tao Zhang and De-Zheng Sun

**Cooperative Institute for Research in Environmental Sciences**
**University of Colorado/NOAA Earth System Research Laboratory**
**Physical Sciences Division**
**Boulder, Colorado**

(*Submitted to Journal of Climate*)

July 29, 2013

Corresponding author address:
Dr. Tao Zhang
NOAA/ESRL/PSD
325 Broadway, R/PSD1
Boulder, CO 80305
Email: tao.zhang@noaa.gov

## Abstract

The El Niño–La Niña asymmetry is evaluated in fourteen CMIP5 coupled models. The results show that an underestimate of ENSO asymmetry is a common problem in CMIP5 coupled models. The underestimate of the asymmetry also shows up in zonal wind stress, precipitation and subsurface temperature. The weaker SST warm anomalies and the westward shift of maximum center over the eastern Pacific are the main contributors to the weaker ENSO asymmetry in coupled models. Generally, SST anomalies for the La Niña phase are realistically simulated in CMIP5 coupled models.

SST-forced AMIP runs are analyzed to understand the cause for the underestimate of ENSO asymmetry in coupled models from the atmospheric origin. We found that during the warm phase, precipitation anomalies are too weak over the eastern Pacific and westerly wind anomalies have less shift to the east in most models. The time-mean zonal winds are stronger over the equatorial central and eastern Pacific for most models. Wind-forced ocean GCM experiments suggest that the stronger time-mean zonal winds and weaker asymmetry in the inter-annual anomalies of the zonal winds in AMIP models can both be a contributing factor to a weaker ENSO asymmetry in the corresponding coupled models, but the former appears to be a more fundamental factor, possibly through its impact on the mean state. The study suggests that the underestimate of ENSO asymmetry in the CMIP5 coupled models is at least in part of atmospheric origin.

## 1. Introduction

The El Niño–Southern Oscillation (ENSO), which has widespread effects on the weather and climate globally (Ropelewski and Halpert 1987; Kiladis and Diaz 1989; Hoerling et al. 1997; Larkin and Harrison 2005; Zhang et al. 2011), is the dominant driver for interannual climate variability. On the interannual timescales, the tropical Pacific SST is fluctuating with positive anomalies during warm (El Niño) phase and negative anomalies during cold (La Niña) phase. The two phases of ENSO are not mirror images of each other and the magnitude of SST anomalies over the eastern equatorial Pacific is larger during warm phase compared to cold phase, causing a non-zero residual effect or a positive ENSO asymmetry (Burgers and Stephenson 1999).

The asymmetry between two phases of ENSO shows up in both the surface fields as well as in the subsurface fields (Rodgers et al. 2004; Schopf and Burgman 2006; Sun and Zhang 2006; Zhang et al. 2009). Causes for such an asymmetry are not yet clearly understood, but many studies suggest that it is likely a consequence of nonlinearity of the ocean dynamics (Jin et al. 2003; An and Jin 2004; Su et al. 2010). By the analysis of the heat budget of the ocean surface layer, Jin et al. (2003) and An and Jin (2004) found that the nonlinear vertical temperature advections are a major contributor to the ENSO amplitude asymmetry. However, based on the updated ocean assimilation products, Su et al. (2010) suggested that the nonlinear zonal and meridional ocean temperature advections are essential to cause the asymmetry in the far eastern Pacific, while the vertical nonlinear advection has the opposite effect. Another possible cause for the ENSO asymmetry is the asymmetric negative feedback due to the tropical ocean instability waves in the eastern Pacific that has a relatively stronger impact on the La Niña than El

Niño (Vialard et al. 2001). Kang and Kug (2002) argued that the relatively weak SST anomalies during La Niña compared to those of El Niño are associated with a westward shift of zonal wind stress anomalies, which is in turn attributed to the nonlinear dependence of deep convection on the SST as noted by Hoerling et al. (1997). These suggested major physics mechanisms responsible for the asymmetry between El Niño and La Niña are also described in a review study of An (2009).

El Niño–La Niña asymmetry is also linked to the time-mean effect of ENSO (Sun and Zhang 2006; Schopf and Burgman 2006; Sun 2010, Liang et al. 2012). By using a coupled model to conduct numerical experiments with and without ENSO, Sun and Zhang (2006) demonstrated that ENSO works as a basin-scale mixer to regulate the time-mean thermal stratification in the upper-equatorial Pacific. Schopf and Burgman (2006) proposed a kinematic effect of oscillating a nonlinear temperature profile to account for the long-term mean state as the ENSO amplitude changes. Understanding the causes and consequences of ENSO asymmetry may hold the key to understand decadal variability in the tropics and beyond (Rodgers et al. 2004; Sun and Yu 2009; Liang et al. 2012). In order to fully capture the role of ENSO in the climate system, the climate models need to simulate well the asymmetry of ENSO.

The ENSO asymmetry in coupled models has been extensively examined in previous studies (Burgers and Stephenson 1999; Hannachi et al. 2003; An et al. 2005; van Oldenborgh et al. 2005; Zhang et al. 2009). Measured by the skewness (Burgers and Stephenson 1999; Hannachi et al. 2003) or the asymmetricity (variance-weighted skewness) (An et al. 2005) of SST anomalies in the Niño-3 region (90$^{o}$W-150$^{o}$W, 5$^{o}$S-5$^{o}$N), most models are found to underestimate the observed positive ENSO asymmetry.

However, those studies only focus on the evaluation of ENSO asymmetry in the coupled models and barely attempt to understand the weaker ENSO asymmetry separate from the bias in the stand-alone atmosphere model. In the complex coupled system it is difficult to identify the causes for the bias in ENSO asymmetry due to the coupled ocean-atmosphere feedbacks involved. By analyzing previous NCAR coupled models (CCSM1, CCSM2, CCSM3 at T42, CCSM3 at T85, and CCSM3+NR) in conjunction with the corresponding Atmospheric Model Intercomparison Project (AMIP) runs, Zhang et al. (2009) showed that all the models underestimate the observed ENSO asymmetry, but CCSM3+NR with Neale and Richter convection scheme (Neale et al. 2008) has significant improvements over the earlier versions with Zhang and McFarlane convection scheme (Zhang and McFarlane 1995). Enhanced convection over the eastern Pacific during the warm phase of ENSO appears to be the cause for the improvement. Zhang et al. (2009) also noted a warmer SST climatology in CCSM3+NR in contrast to other versions.

The purpose of this study is to evaluate the ENSO asymmetry in CMIP5 coupled models including the surface and subsurface signatures by extending the analysis in previous NCAR models. We attempt to test the hypothesis developed from previous analysis of NCAR models (Zhang et al. 2009) against the results from CMIP5 models (Taylor et al. 2012). We will explore whether the underestimate of ENSO asymmetry remains a common problem in the state-of-art coupled model; whether the underestimate of ENSO asymmetry in CMIP5 models is related to the weaker convection over the eastern Pacific during warm phase; and whether the mean SST state is important to ENSO asymmetry.

119 This paper is organized as follows. We introduce the observational and model data
120 sets as well as the methodology of our analysis in section 2. We present the analysis of
121 ENSO asymmetry in CMIP5 models in the coupled runs, and then the asymmetry in the
122 corresponding AMIP runs. To understand the effect of bias in the atmospheric response
123 on ENSO asymmetry in coupled models, the numerical experiments forced by AMIP
124 winds are conducted in section 3. Conclusions and discussions are presented in the last
125 section.
126

127 ## 2. Data and Methods

128 The ENSO asymmetry in fourteen coupled ocean-atmosphere models from CMIP5
129 control runs (piControl) has been evaluated in this investigation. Presented here are the
130 results from the coupled models whose corresponding AMIP runs are available for the
131 analysis. We will first assess the ENSO asymmetry in the SST and then look at the
132 asymmetry in upper ocean temperature in the models. We further analyze the
133 corresponding fields of precipitation and surface wind stress in the coupled runs to
134 understand whether the bias in ENSO asymmetry is linked to the bias in precipitation and
135 associated surface wind stress. The corresponding AMIP runs from CMIP5 models are
136 also examined to understand whether the biases in precipitation and surface wind stress in
137 coupled runs stem from the biases in stand-alone atmosphere models.
138 In addition to analyzing the asymmetry in the CMIP5 AMIP runs, we also use the
139 NCAR Pacific basin model to perform the forced ocean experiments driven by CMIP5
140 AMIP winds. Our model is the one used by Sun (2003), Sun et al. (2004) and Sun and
141 Zhang (2006). The model uses the NCAR Pacific basin model (Gent and Cane, 1989) as

its ocean component. The model calculates the upper ocean temperatures based on first principles and simulates well the observed characteristics of ENSO in both the forced and coupled modes (Sun 2003). We will compare the ENSO asymmetry in the runs forced by AMIP winds with that by observed winds to understand the effect of the bias in the atmospheric response on ENSO asymmetry in CMIP5 coupled models.

The observational data used for examining the model results are the same as those used by Zhang et al. (2009). The SST data from the Hadley Centre Sea Ice and SST (HadISST) dataset (Rayner et al. 2003) are used for evaluating the asymmetry in the SST field in the CMIP5 coupled models. The simple ocean data assimilation (SODA) set (Carton et al. 2000) is used for validating the upper-ocean temperature in the models. Precipitation data are obtained from the Climate Prediction Center (CPC) Merged Analysis of Precipitation (CMAP; Xie and Arkin 1997). The wind stress data are obtained from the simple ocean data assimilation (SODA) set (Carton and Giese 2008) in which the surface winds are a combination of ERA-40 and Quick Scatterometer (QuikSCAT) satellite observations.

We will use the skewness (Burgers and Stephenson 1999) of interannual variability of SST to quantify the ENSO asymmetry. We will also conduct the composites of El Niño and La Niña and then use the sum of the composite between two phases of ENSO to measure the asymmetry. The definition of the warm phase and cold phase of ENSO follows that of Zhang et al. (2009). The composite analysis will help to identify which phase of ENSO the bias in ENSO asymmetry mainly originates from.

## 3. Results

### *a. Asymmetry in the coupled models*

A quantitative measure of the ENSO asymmetry in CMIP5 coupled models reveals that an underestimate of the ENSO asymmetry remains a common bias in our state-of-the-art climate models. Figure 1 shows the skewness of Niño-3 SST anomalies from observations and the models, together with their variance. Measured by the variance of Niño-3 SST, ENSO in many models is as strong as in observations. But measured by the skewness of Niño-3 SST, all the coupled models that we have analyzed underestimate the observed positive ENSO asymmetry. This indicates that the observed SST anomalies in the eastern Pacific are skewed toward warm events, while those in coupled models have a more Gaussian-like distribution. In comparison, the NCAR CCSM4 model (Gent et al. 2011; Deser et al. 2012) stands out as the best model in simulating the ENSO asymmetry, whose variability of ENSO is also comparable to observations. The HadGEM2-ES model, which also has a comparable ENSO variability to observations, is found to have the largest bias in reproducing the observed positive skewness, because it shows a strong negative skewness, contrary to observations. The results suggest that the stronger variability of ENSO (measured by variance) does not guarantee a stronger asymmetry (measured by skewness) in CMIP5 coupled models.

Figure 2 shows the sum of the SST anomalies between the warm and cold phases of ENSO from observations and coupled runs from CMIP5. This sum has also been called SST anomaly residual and is a common measure of the ENSO asymmetry in the SST field. The SST anomaly residual results are similar to the skewness map of SST anomalies (not shown). All the CMIP5 models evaluated underestimate the observed positive SST residual and, therefore, the asymmetry over the eastern Pacific, consistent

188 with the results of skewness. There is an obvious negative SST residual over the eastern
189 Pacific in HadGEM2-ES model, in agreement with a considerable negative skewness of
190 Niño-3 SST anomalies in this model (Figure 1). Generally, CCSM4 model has a better
191 simulation of the positive SST residual in the eastern Pacific than other models, which is
192 also confirmed by the skewness results noted earlier. Despite the fact that all the models
193 underestimate the positive SST residual over the eastern Pacific, the overestimate of the
194 negative SST residual in the western Pacific is evident in many models (e.g. GISS-E2-R,
195 MIROC5, CSIRO-MK3-6-0, CCSM4).

196 As already noted in the analysis of the previous NCAR models and consistent with
197 earlier understanding of ENSO dynamics, the asymmetry in the subsurface temperature is
198 more profound than in the surface (Zhang et al. 2009). To obtain more information about
199 the cause for the bias in simulated ENSO asymmetry, we look at the asymmetry of the
200 subsurface signal. Figure 3 shows the sum of the equatorial upper-ocean temperature
201 anomalies between the warm and cold phases of ENSO from observations and coupled
202 runs from CMIP5 models. The observed subsurface temperature shows a positive
203 asymmetry of about 1°C around 75-m depth over the eastern Pacific and a negative
204 asymmetry of about -0.4°C around 150-m depth over the western Pacific. All the models
205 underestimate the positive asymmetry in the subsurface temperature over the eastern
206 Pacific. In contrast to the asymmetry in SST, the underestimate of the positive asymmetry
207 in the subsurface temperature is more profound over the eastern Pacific (note the
208 different scale in Figure 2 and Figure 3). Most models also have a weaker negative
209 asymmetry in the subsurface over the western Pacific. Despite the comparable magnitude
210 to observations, the negative asymmetry over the western Pacific extends too far to the

211 east in some models (CNRM-CM5, FGOALS-g2, CCSM4). There is a good match
212 between SST and subsurface temperature for the negative asymmetry in HadGEM2-ES
213 over the eastern Pacific (Figure 3 and Figure 2). Consistent with the stronger positive
214 SST residual over the eastern Pacific, CCSM4 also has a stronger positive residual in the
215 subsurface. Again, the bias in SST asymmetry appears to be linked to the bias in the
216 asymmetry of the subsurface temperature, as noted in Zhang et al. (2009).

217 To explore which phase of ENSO is the major source for the weaker residual in the
218 SST and the subsurface in CMIP5 models, we investigate the spatial distribution of
219 composite anomalies during two phases of ENSO. Figure 4 gives the spatial pattern of
220 composite SST anomalies during the warm phase of ENSO. Observations show that the
221 stronger positive SST anomalies associated with warm events are located over the South
222 American coast and the maximum value can reach about 1.6°C. Most models have a
223 weaker SST warm anomaly over the eastern Pacific, and the underestimate of the warm
224 SST anomaly is more serious in the coastal regions (100°W-80°W). The simulated
225 maximum center is found to shift westward in many models. These biases contribute to
226 the weak SST residual in the models (Figure 2). The observed maximum center around
227 110°W is well captured in CCSM4 model that has an enhanced warm anomaly over the
228 coastal regions which contributes to the increase in SST residual (Figure 2).

229 The bias in the warm anomalies also shows up in the subsurface (Figure 5).
230 Consistent with the bias in the SST warm anomalies, most models have a weaker
231 subsurface warm anomaly over the eastern Pacific and the simulated maximum center is
232 shifted westward. The better simulation of SST warm anomalies in CCSM4 model is
233 apparently associated with the improvement in the simulation of warm anomalies of

234 subsurface temperature. Over the western Pacific, the underestimate of the negative
235 anomalies in the subsurface is also evident in many models. The negative anomalies in
236 the subsurface over the western Pacific in NorESM1-M model are much stronger and
237 extend too far to the east during the warm phase, causing a more stronger and eastward
238 extended negative asymmetry in this model (Figure 3).

239 To better understand the cause for the underestimate of the skewness in CMIP5
240 coupled models, the probability distribution function (PDF) pattern of Niño-3 SST
241 anomalies from observations and CMIP5 coupled models is displayed in Figure 6. The
242 observed maximum positive anomalies are about 3.5°C but the maximum negative
243 anomalies are about -2°C, in agreement with the observed positive skewness (Figure 1).
244 With the exception of CCSM4 model, all the CMIP5 models underestimate the observed
245 warm anomalies and the maximum bias in the underestimate is close to 2°C. Compared
246 to observations, the models do not bias toward the same direction for the cold anomalies
247 and the bias during the cold phase is relatively small (about 0.5~1°C). The ensemble
248 mean results indicate that the underestimate of the warm anomalies is the major cause for
249 the weaker ENSO asymmetry in CMIP5 coupled models.

250 Figure 7 further shows the sum between the warm composite anomalies and cold
251 composite anomalies in precipitation (shaded) and zonal wind stress (contours) from
252 observations and coupled models. The observed precipitation is characterized by a strong
253 positive asymmetry in the central and eastern Pacific and a strong negative asymmetry in
254 the western Pacific, resulting from the westward shift during the cold phase compared to
255 the warm phase (Zhang et al. 2009). The underestimate of the positive precipitation
256 asymmetry over the central and eastern Pacific is prominent in the models. Consistent

with the weak asymmetry in the precipitation, the asymmetry in zonal wind stress is also weak in the coupled models, which is expected from the weak asymmetry in the subsurface temperature noted earlier. The bias in zonal wind stress revealed in the previous CMIP3 models is also found to be responsible for the weaker SST skewness in CMIP3 models. Van Oldenborgh et al. (2005) suggested that the weaker response in zonal wind stress over the central and eastern Pacific in most models explains the general lower thermocline variability than observed and will also suppress the nonlinear aspects of ENSO in the ocean in CMIP3 coupled models.

*b. Asymmetry in the AMIP runs*

To understand whether the weaker asymmetry in precipitation and wind stress in CMIP5 coupled models is a consequence of the corresponding SST fields or the cause of the latter, we perform the composite analysis from the corresponding AMIP runs of CMIP5 models that are forced by the observed SST boundary conditions. The AMIP runs involve subjecting the atmospheric component of CMIP5 coupled models to the observed ENSO SST variability and thus specifying the full ENSO asymmetry. The specification of the observed ENSO conditions in the AGCMs greatly increases the asymmetry in tropical Pacific rainfall, especially over the central Pacific where the AMIP results are in much better agreement with observations than the results from coupled runs (Figure 8). However, most models have a weaker precipitation asymmetry over the eastern Pacific. The NCAR model, which has proved to be the best model in simulating the ENSO asymmetry, is found to have a comparable precipitation asymmetry in the eastern Pacific. This suggests that the realistic simulation of precipitation asymmetry in the eastern Pacific may be an important factor for a better simulation of ENSO asymmetry.

Figure 9 shows a quantitative measure of the precipitation asymmetry over the eastern Pacific. The top panel is results from the coupled runs and the bottom panel is those from the corresponding AMIP runs. All the coupled models have a weaker precipitation asymmetry over the eastern Pacific. By comparison, the CCSM4 coupled model has the largest value of precipitation asymmetry. The increase in precipitation asymmetry from coupled runs to AMIP runs is also evident over the eastern Pacific. We also note that nine of fourteen AMIP models have a weaker precipitation asymmetry over the eastern Pacific even driven by the observed SST forcing. Two AMIP models (NorESM1-M and MRI-CGCM3) have a comparable precipitation asymmetry to the observed and the other three AMIP models (GISS-E2-R, CCSM4, and bcc-csm1-1) have a slightly larger precipitation asymmetry. The error of the weaker asymmetry in precipitation is apparently amplified in coupled runs as the coupled runs are found to have a much weaker precipitation asymmetry than their corresponding AMIP runs. There is a positive correlation (0.58) for the precipitation asymmetry averaged over the eastern Pacific between fourteen AMIP runs and coupled runs. The weak precipitation asymmetry over the eastern Pacific is mainly due to the bias in the warm phase (Figure 10). Nine of fourteen AMIP models have a weaker precipitation warm anomaly over the eastern Pacific. The precipitation warm anomaly is well captured in three models (HadGEM2-ES, MRI-CGCM3, and bcc-csm1-1) and somewhat overestimated in the other two models (GISS-E2-R, and CCSM4). Again, the corresponding coupled models have a much weaker precipitation warm anomaly and all the coupled models underestimate the observed precipitation warm anomaly. This seems to indicate that the insufficient precipitation response to El Niño warming over the eastern Pacific is an intrinsic error of the majority of the atmospheric

303 models.

304 Figure 11 further shows the spatial pattern during the warm phase for observations,
305 the ensemble mean AMIP runs, and the differences between them. The left panel shows
306 the precipitation and the right one the zonal wind stress. Consistent with the results
307 shown in Figure 10 bottom, there is a weaker precipitation response over the eastern
308 Pacific in the AMIP runs. Note that the precipitation warm anomalies in the AMIP runs
309 are somewhat stronger over the central Pacific, and this positive bias is also reflected in
310 the precipitation residual (Figure 8), further confirming that the bias in the warm phase of
311 ENSO is the major source for the bias in ENSO asymmetry. In contrast to observations,
312 the precipitation response shows a less eastward extension (indicated by shaded values)
313 in the AMIP runs during the warm phase. Linked to the precipitation response, the
314 westerly wind (positive) anomaly is positioned too far to the west and shifts westward by
315 about $10^{o}$ (indicated by green lines shown on Figure 11 right panel, top two). Similar to
316 the precipitation difference, there is an obvious negative (weaker westerly wind) anomaly
317 over the eastern Pacific and a positive (stronger westerly wind) anomaly over the central
318 Pacific (Figure 11 right panel, bottom). The westward shift of the zonal wind stress warm
319 anomalies in the AMIP runs may contribute to the weaker warm anomaly of subsurface
320 temperature in most coupled models during the warm phase (Kang and Kug 2002).

321 The CMIP5 AMIP runs are found to have biases in the mean zonal winds over the
322 equatorial central and eastern Pacific and in the asymmetry in the central Pacific wind
323 variability (Figure 12). Eleven of fourteen models have a stronger mean zonal wind in
324 AMIP runs, and the other three models (HadGEM2-ES, CCSM4 and CSIRO-MK3-6-0)
325 have a comparable mean wind to the observed. Ten of fourteen models underestimate the

observed positive skewness of central Pacific zonal winds in AMIP runs. Models CNRM-CM5 and bcc-csm1-1 have a better simulation of the observed wind skewness, while models IPSL-CM5A-LR and MPI-ESM-LR have a stronger skewness in the zonal wind stress and the mean winds are also much stronger in these two models, especially in the latter. Generally, the ensemble mean results show that the AMIP runs have a stronger mean winds and a weaker skewness in the zonal winds.

The spatial map of time mean zonal wind stress shows that there is a stronger mean wind in the model over most regions of the equatorial Pacific (Figure 13). The bias in the mean wind (negative values) is more significant in the coastal regions (110$^{o}$W-90$^{o}$W, 0-10$^{o}$N), where the mean precipitation is also much underestimated in the AMIP run. The stronger tropical winds are accompanied with excessive precipitation over much of the tropics, especially over the regions off the equator. The similar biases in winds and precipitation were also found in the previous CMIP3 AMIP runs (Lin 2007). There is a clear east-west asymmetry in the precipitation bias and the resulting excessive zonal latent heating gradient associated with zonal precipitation gradient may drive the stronger winds in the model (Lin 2007). The biases in the surface winds from AMIP runs play a role in the ENSO asymmetry, which will be shown by the following numerical experiments.

*c. Numerical experiments*

To understand the biases of model winds associated with convection in AMIP runs on the ENSO asymmetry in CMIP5 coupled models, we use the NCAR Pacific basin model (Sun 2003; Sun et al. 2004; Sun and Zhang 2006) to perform numerical experiments. We conduct the forced ocean model experiments with the use of ensemble mean AMIP winds

349 from fourteen CMIP5 models and compare the results with those from the forced ocean
350 runs driven by the observed wind stress. Four groups of numerical experiments combined
351 with different climatology and interannual anomalies of winds in observations and
352 ensemble mean AMIP runs of CMIP5 models are listed in Table 1. We first perform the
353 forced ocean experiments with both climatology winds and interannual anomalies of
354 winds from observations (Experiment I). To understand the role of climatology winds in
355 the models, we then replace the observed climatology winds by the modeled climatology
356 winds but keep the observed interannual anomalies of winds unchanged in the forced
357 experiments (Experiment II). Next, we use the actual AMIP model winds that include the
358 simulated climatology and interannual anomalies to drive the ocean model, which will
359 further explore the role of modeled interannual anomalies in the surface winds on ENSO
360 asymmetry (Experiment III). Finally, to explore the role of observed climatology winds,
361 we replace the modeled climatology winds with the observed climatology winds but keep
362 the modeled interannual anomalies of winds to drive the ocean (Experiment IV). These
363 experiments are designed to probe the relative role of the bias in climatology winds and
364 interannual variability of winds in AMIP runs in causing the underestimate of ENSO
365 asymmetry in CMIP5 coupled runs.

366 Table 1 shows the standard deviation and skewness of the interannual variability in
367 Niño-3 SST from four forced ocean runs. Driven by observed winds (Experiment I), the
368 model can well reproduce the observed skewness value of Niño-3 SST anomalies. The
369 skewness value of 1.16 in Experiment I is very close to the observed skewness value of
370 1.05 over the same 30-year period. The results in the table show that the skewness from
371 the run forced by full model winds (0.70 in Experiment III) is about 40% weaker than

372 that from the run by the observed winds (1.16 in Experiment I) accompanied by a
373 weakened variability. By comparing the results from two cases that use the same
374 observed wind anomaly but different wind climatology (Experiment I and Experiment II),
375 we find the bias in the modeled wind climatology is partially (~50%) responsible for the
376 reduction in the ENSO asymmetry. The use of simulated wind interannual anomalies will
377 further reduce the ENSO asymmetry, as the skewness in the run with full model winds is
378 the smallest (Experiment III). Interestingly, we note that the skewness in the case with
379 observed wind climatology but keeping simulated wind interannual anomalies
380 (Experiment IV) is comparable to that in the run by the observed full winds (Experiment
381 I), although the variability remains weak. The results from Experiments III and IV
382 indicate that the improvement in mean winds play a dominant role in improving the
383 simulation of ENSO asymmetry.

384 To further explore the cause for the difference in the skewness in the runs listed in
385 Table 1, the probability distribution function (PDF) pattern of Niño-3 SST anomalies
386 from four forced ocean experiments is shown in Figure 14. Consistent with the results in
387 Table 1, the Niño-3 SST anomalies in the run driven by observed winds (black line) show
388 a stronger positive skewness. The maximum positive anomaly can reach 3°C and the
389 maximum negative anomaly is limited to about -1.6 °C. When the climatology winds
390 from models are used to replace the observed wind climatology, the stronger warm
391 anomalies (2°C~3°C) start to decrease while there is an increase in the warm anomalies
392 of 1.6°C ~ 2°C (blue line). The increase in the cold anomalies of -1.25°C ~ -0.75°C
393 contributes to a slightly weaker skewness in the run forced by modeled wind climatology
394 and observed wind interannual anomaly (Experiment II). The underestimate of the warm

anomalies is more serious in the run with both modeled wind climatology and modeled wind interannual anomaly (green line), in agreement with the smallest skewness listed in Table 1. This also suggests that the biases in both climatology and interannual anomaly of AMIP model winds account for the weaker ENSO asymmetry in CMIP5 models. Comparing the results from Experiments III and IV, we find that replacing modeled wind climatology with observed wind climatology causes an overall increase in the stronger warm anomalies (2°C~3°C) and a decrease of the maximum negative anomaly from -2°C to -1.6°C, which is responsible for the increase in skewness (red line).

The residual pattern of SST shows that there is a progressive decrease in the positive SST residual over the Niño-3 region from Experiment I to Experiment III (Figure 15) consistent with the skewness value shown in Table 1. The decrease in the positive SST residual is more obvious in Experiment III when full model winds are used. There is also a gradual westward shift in the positive SST residual, and the westward shift is also visible in the subsurface. The positive SST residual over the Niño-3 region is greatly increased from Experiment III to Experiment IV when observed mean winds are used to replace the modeled mean winds, although there is a lack of evident positive SST residual over the coast regions (100°W-80°W) in these two cases. Thus compared to observed wind anomalies, the wind anomalies in models can reduce the positive SST residual over the coast regions.

Figure 16 shows the spatial map of the composite anomalies of SST (left panel) and the equatorial upper ocean temperature (right panel) during the warm phase of ENSO from four forced ocean experiments. The NCAR Pacific basin model used in this study reproduces the pattern of observed SST warm anomalies (Figure 4). The simulated

418 stronger SST warm anomalies in the run forced by observed winds (top left) are located
419 over the South American coast. The bias in the modeled wind climatology causes a slight
420 westward shift of stronger SST warm anomaly but does not reduce the magnitude
421 (second row left). Accompanied with a weaker subsurface temperature warm anomaly
422 (third row right), the westward shift of SST warm anomaly is more evident and the
423 magnitude of SST warm anomaly becomes weaker if the bias in the interannual anomaly
424 of modeled winds is also involved (third row left). The features of SST and subsurface
425 temperature warm anomalies in the run forced by full model winds also exist in CMIP5
426 coupled models (Figure 4 and Figure 5). The comparison between Experiments III and IV
427 shows that changing mean winds from models to observations alone can increase SST
428 warm anomalies. Due to the use of the same model wind anomalies, the westward shift of
429 SST warm anomaly is still evident in Experiment IV. This is consistent with the lack of
430 positive SST residual over the coast regions noted earlier (Figure 15).

431 During the cold phase of ENSO (Figure 17), bias in the modeled wind climatology
432 somewhat increases the magnitude of cold SST anomalies over the Niño-3 region and
433 thus reduces the SST skewness. The increase in cold SST anomaly magnitude is linked to
434 the stronger cold subsurface temperature (second row). Interestingly, the inclusion of
435 wind anomalies from models is found to significantly reduce the magnitude of SST warm
436 anomalies, but does not deteriorate the bias in cold SST anomalies (third row). Instead,
437 the cold SST anomalies and subsurface temperature anomalies are comparable to those in
438 the run forced by observed full winds. This also supports the previous analysis that the
439 underestimate of the SST skewness in CMIP5 models is mostly due to bias in the warm
440 phase. The Experiment IV results show that the observed mean winds can reduce the cold

441 SST anomalies, favoring an increase of SST skewness. Among the four runs, Experiment
442 IV has a more confined cold SST anomaly within the equatorial Pacific, while the other
443 three runs show a more meridional extension of the cold SST anomalies, especially
444 over the southern equatorial Pacific. The weakened cold SST anomalies over the Niño-3
445 region in Experiment IV is linked to the reduction in cold subsurface temperature
446 anomalies.

447 Figure 18 shows the time-mean SST difference and the equatorial upper ocean
448 temperature difference of Experiments II, III, IV from Experiment I. Compared to
449 Experiment I, there is a stronger cold SST over the cold-tongue regions in Experiments II
450 and III, in which the observed mean winds are replaced with mean winds from models.
451 The subsurface temperature is also colder in these two cases that have a weaker SST
452 skewness. By comparison, the SST and subsurface temperature in Experiment IV are
453 comparable to those in Experiment I, since these cases use the same observed mean
454 winds.

455 Note that different from Experiment I, Experiment IV uses the interannual anomalies
456 of winds from models but still has a comparable SST skewness to the observed. This
457 suggests that the mean SST state induced by mean winds is fundamentally important to
458 the simulation of ENSO asymmetry, and the bias in wind variability is secondary.

459 In general, the effect of the bias in interannual anomalies of modeled winds on ENSO
460 asymmetry is mainly attributed to wind bias in the warm phase—a westward shift of the
461 zonal wind stress warm anomalies in the AMIP runs, linked to the insufficient
462 precipitation response over the eastern Pacific during the warm phase (Figure 11). These
463 numerical experiments demonstrate that when there is a colder mean SST state due to the

464 stronger mean winds in models, the biases in interannual anomalies of winds from AMIP
465 runs can weaken ENSO asymmetry by shifting SST warm anomalies westward and
466 reducing their magnitude. When there is a warmer mean SST state, or the model mean
467 winds are the same as observations, the ENSO asymmetry can be as large as that in the
468 run with observed full winds, and the contribution to ENSO asymmetry from the bias in
469 wind interannual variability is small.
470

471 **4. Summary**

472 In this study, we evaluated the fidelity of CMIP5 coupled models in simulating the
473 ENSO asymmetry by extending the analysis in the previous NCAR models (Zhang et al.
474 2009). Furthermore, causes for bias in ENSO asymmetry in CMIP5 coupled models are
475 explored by analyzing the corresponding AMIP runs of CMIP5 coupled models and by
476 conducting forced ocean GCM experiments with the winds from CMIP5 AMIP runs

477 Previous analysis of CMIP3 coupled models noted that, different from observations,
478 most coupled models have a near zero SST skewness in the tropical Pacific and a linear
479 ENSO (van Oldenborgh et al. 2005; Sun et al. 2013). The present findings show that the
480 underestimate of observed positive ENSO asymmetry measured by skewness is still a
481 common problem in CMIP5 coupled models, although many models have comparable
482 variance in Niño-3 SST with respect to observations. When the asymmetry is measured
483 by the SST residual between the two phases of ENSO, all the models are also found to
484 have a weaker ENSO asymmetry than observations. The underestimate of the asymmetry
485 in the subsurface temperature is more profound than that in the SST field in the CMIP5
486 coupled models. The underestimate of the asymmetry in the subsurface signature is

consistent with the weaker asymmetry in the zonal wind stress, which is associated with the weaker asymmetry in the precipitation. The composite analysis indicates that the bias during the warm phase of ENSO is the major contributor to the weaker asymmetry of ENSO in CMIP5 coupled models. The SST warm anomalies over the far eastern Pacific are found to be weaker in the coupled models than in observations and the simulated maximum warm SST center over the eastern Pacific shifts westward. Examining the subsurface temperature warm anomalies reveals the same bias—most models have a weaker subsurface temperature warm anomaly over the eastern Pacific and the maximum center shifts westward. The underestimate of the negative anomaly in the subsurface over the western Pacific is also evident in many coupled models.

The asymmetry in the precipitation and zonal wind stress from the corresponding AMIP runs are first analyzed to understand the causes for the weaker ENSO asymmetry in CMIP5 coupled models. We found that mainly due to the weaker precipitation response to El Niño warming, most models have a weaker precipitation asymmetry over the eastern Pacific even driven by the observed SST forcing. This bias is further amplified in the coupled models that have a much weaker precipitation asymmetry over the eastern Pacific. During the warm phase, the weaker precipitation response over the eastern Pacific is accompanied by a stronger precipitation response over the central Pacific and linked to a westward shift of convection in the AMIP runs along with a clear westward shift of westerly wind anomaly. Compared to observations, the westward shift of zonal wind stress during the warm phase in the AMIP runs may play a role in the weaker subsurface temperature warm anomalies in the coupled models (Kang and Kug 2002). Using two different coupled models to examine the sensitivity of ENSO amplitude

510 to the convection scheme parameters, Watanabe et al. (2011) and Kim et al. (2011)
511 showed that the parameter change in the cumulus parameterization shifts the position of
512 the precipitation anomalies and the zonal wind stress also shifts accordingly. The
513 increased eastern Pacific precipitation tends to shift the wind stress anomalies to the east.
514 Closer to the eastern Pacific, the wind stress forcing more effectively deepens the
515 thermocline over the eastern Pacific. Watanabe et al. (2011) also demonstrated that the
516 subsurface temperature anomalies over the eastern Pacific are much stronger when the
517 zonal wind stress shifts to the east. This is consistent with what we see from the CCSM4
518 model. The NCAR model, identified as the best model in simulating ENSO asymmetry,
519 has a realistic simulation of subsurface temperature warm anomalies associated with
520 sufficient precipitation response over the eastern Pacific in the AMIP run. An enhanced
521 precipitation response over the eastern Pacific during the warm phase is essential to the
522 improvement in the simulation of ENSO asymmetry in CMIP5 models, consistent with
523 the previous findings of Zhang et al. (2009).

524 We also find that AMIP runs have biases in both the time-mean zonal winds over the
525 equatorial central and eastern Pacific, and the asymmetry in the central Pacific wind
526 variability. Most models have a stronger mean zonal wind and underestimate the
527 observed positive skewness of zonal winds. The bias in the mean zonal winds is more
528 prominent in the coastal regions over the eastern Pacific and the southern equatorial
529 Pacific, where the bias in mean precipitation is also evident in the AMIP runs. The mean
530 precipitation bias shows an east-west asymmetry. The latent heating asymmetry
531 associated with the stronger zonal precipitation gradient may generate the stronger zonal
532 pressure gradient force which then enhances the trade winds in the model (Lin 2007).

533 To understand the effect of the bias in the mean and interannual variability of winds
534 on ENSO asymmetry, forced ocean model experiments with the use of AMIP winds are
535 performed. These results are compared to those from the experiments forced by observed
536 winds. The numerical experiments show that when there is a colder mean SST state due
537 to the stronger mean winds in models, the biases in interannual anomalies of winds from
538 AMIP runs can weaken ENSO asymmetry by shifting SST warm anomalies westward
539 and reducing the magnitude. This is consistent with what we have seen in CMIP5
540 coupled models. The results from the run with full model winds confirm that the bias in
541 the SST anomalies during the warm phase is found to be the major cause for the
542 reduction in ENSO asymmetry. We note that with a warmer mean SST state, or when the
543 mean winds in models are the same as observations, the contribution to ENSO
544 asymmetry from wind interannual variability bias is negligible. Also ENSO asymmetry is
545 significantly increased mainly due to the increase of SST warm anomalies. The results
546 are consistent with those from an analytical model that the amplitude of warm events
547 increases with enhanced radiative heating (Liang et al. 2012). This may also be useful to
548 explain why coupled models tend to have a weaker ENSO asymmetry, given that the
549 excessive cold tongue is still the problem in coupled models (Sun et al. 2006). These
550 findings highlight the importance of a warmer mean SST state to ENSO asymmetry. It
551 suggests that improving the mean winds in the atmosphere model is a key step to better
552 simulate the ENSO asymmetry in CMIP5 models.

553 It should be noted that we fully consider the momentum forcing (both zonal and
554 meridional components) from AMIP model winds in the experimental design as an
555 attempt to reveal the role of the bias in model winds more realistically. We have also

556 performed additional ocean model experiments in which only zonal wind stress biases are
557 considered. The results are found to be similar, suggesting a minor role of the biases in
558 meridional wind stress. The meridional wind stress anomalies are not important in ENSO
559 because they can not efficiently excite the oceanic Kelvin wave, one of the key dynamic
560 processes in ENSO events (McCreary 1976; Zhang and McPhaden 2006). Using a high-
561 resolution Ocean General Circulation Model (OGCM) to examine the role of meridional
562 wind stress anomalies in ENSO simulations, Zhu et al. (2007) shows that changes in the
563 direction and magnitude of meridional wind stress anomalies have little influence on
564 ENSO simulations until the anomalies are unrealistically enlarged by a factor of 5.

565 It is thus reasonable to argue that the weaker ENSO asymmetry in CMIP5 coupled
566 models may be linked to the bias in the winds, especially the time-mean winds over the
567 tropical Pacific in the stand-alone atmosphere model. The biases in surface winds in the
568 stand-alone atmosphere model will lead to an initial weaker ENSO asymmetry in the
569 ocean model. The initial bias of a weaker ENSO asymmetry can be amplified in coupled
570 models through the feedbacks between precipitation, surface wind stress, subsurface
571 signatures and SST, resulting in a much weaker ENSO asymmetry as noted in CMIP5
572 coupled models. The role of a possible deficient response from the ocean models to a
573 fixed wind forcing in causing the general underestimate of ENSO asymmetry is not
574 considered in the present study, because the forced CMIP5 ocean models runs with
575 observed wind stress were not available for analysis. A further investigation on the role
576 of ocean dynamics in CMIP5 models is needed to better understand the causes of the bias
577 in the simulated ENSO asymmetry.
578

## Acknowledgments

The authors acknowledge the support of the NOAA Climate Program Office Modeling, Analysis, Predictions and Projections (MAPP) Program as part of the CMIP5 Task Force. Work was supported under grant GC11-300.

584 **References:**

585 An, S.-I., and F.-F. Jin, 2004: Nonlinearity and asymmetry of ENSO. *J. Climate*, **17**,
586 2399–2412.

587 An, S-I., Y-G. Ham, J-S. Kug, F-F. Jin, and I-S. Kang, 2005: El Niño–La Niña
588 asymmetry in the Coupled Model Intercomparison Project simulations. *J. Climate*, **18,**
589 2617–2627.

590 An, S-I., 2009: A review of interdecadal changes in the nonlinearity of the El Nino-
591 Southern Oscillation. *Theor. Appl. Climatol.*, **97,** 29–40.

592 Burgers, G., and D. B. Stephenson, 1999: The "normality" of El Niño. *Geophys. Res.*
593 *Lett.*, **26,** 1027–1030.

594 Carton, J. A., and B. S. Giese, 2008: A reanalysis of ocean climate using Simple Ocean
595 Data Assimilation (SODA). *Mon. Wea. Rev.*, **136,** 2999–3017.

596 Carton, J. A., G. Chepurin, X. Cao, and B. Giese, 2000: A simple ocean data assimilation
597 analysis of the global upper ocean 1950–95. Part I: Methodology. *J. Phys. Oceanogr.*,
598 **30,** 294–309.

599 Deser, Clara, A. S. Phillips, R. A. Tomas, Y. M. Okumura, M. A. Alexander, A.
600 Capotondi, J. D. Scott, Y.-O. Kwon, and M. Ohba, 2012: ENSO and Pacific Decadal
601 Variability in the Community Climate System Model Version 4. *J. Climate*, **25**,
602 2622–2651.

603 Gent, Peter R., G. Danabasoglu, L. J. Donner, M. M. Holland, E. C. Hunke, S. R. Jayne,
604 D. M. Lawrence, R. B. Neale, P. J. Rasch, M. Vertenstein, P. H. Worley, Z.-L. Yang,
605 and M. Zhang, 2011: The Community Climate System Model Version 4. *J. Climate*,
606 **24**, 4973–4991.

607 Gent, P. R., and M. A. Cane, 1989: A reduced gravity, primitive equation model of the
608 upper equatorial ocean, *J. Comput. Phys*., **81**, 444–480.
609 Hannachi, A., D. Stephenson, and K. Sperber, 2003: Probability-based methods for
610 quantifying nonlinearity in the ENSO. *Climate Dyn.*, **20,** 241–256.
611 Hoerling M. P., A. Kumar, and M. Zhong, 1997: El Niño, La Niña, and the nonlinearity
612 of their teleconnections. *J. Climate*, **10**, 1769–1786.
613 Jin, F.-F., S.-I. An, A. Timmermann, and J. Zhao, 2003: Strong El Niño events and
614 nonlinear dynamical heating, *Geophys. Res. Lett*., **30**(3), 1120,
615 doi:10.1029/2002GL016356.
616 Kang, I-S., and J-S. Kug, 2002: El Niño and La Niña sea surface temperature anomalies:
617 Asymmetry characteristics associated with their wind stress anomalies. *J. Geophys.*
618 *Res.*, **107,** 4372. doi:10.1029/2001JD000393.
619 Kiladis, G. N., and H. Diaz, 1989: Global climatic anomalies associated with extremes in
620 the Southern Oscillation. *J. Climate,* **2,** 1069–1090.
621 Kim, D., Y.-S. Jang, D.-H. Kim, Y.-H. Kim, M. Watanabe, F.-F. Jin, and J.-S. Kug
622 (2011), El Niño–Southern Oscillation sensitivity to cumulus entrainment in a coupled
623 general circulation model, *J. Geophys. Res.*, **116**, D22112,
624 doi:10.1029/2011JD016526.
625 Larkin, N. K., and D. E. Harrison, 2005: On the definition of El Niño and associated
626 seasonal average U.S. weather anomalies. *Geophys. Res. Lett.,* **32**, L13705,
627 doi:10.1029/2005GL022738.
628 Liang, J., X.-Q. Yang, and D.-Z. Sun, 2012: The effect of ENSO events on the Tropical
629 Pacific Mean Climate: Insights from an Analytical Model. *J. Climate*, **25**, 7590–7606.

630 Lin, J.-L., 2007: The Double-ITCZ Problem in IPCC AR4 Coupled GCMs: Ocean–
631 Atmosphere Feedback Analysis. *J. Climate*, **20**, 4497–4525.
632 McCreary, J., 1976: Eastern tropical ocean response to changing wind systems: With
633 application to El Niño. *J. Phys. Oceanogr.*, **6,** 632–645.
634 Neale, R. B., J. H. Richter, and M. Jochum, 2008: The impact of convection on ENSO:
635 From a delayed oscillator to a series of events. *J. Climate*, **21,** 5904–5924.
636 Rayner, N. A., D. E. Parker, E. B. Horton, C. K. Folland, L. V. Alexander, D. P. Rowell,
637 E. C. Kent, and A. Kaplan, 2003: Global analyses of sea surface temperature, sea ice
638 and night marine air temperature since the late nineteenth century. *J. Geophys. Res.*,
639 **108,** 4407. doi:10.1029/2002JD002670.
640 Rodgers, K. B., P. Friederichs, and M. Latif, 2004: Tropical Pacific decadal variability
641 and its relation to decadal modulation of ENSO. *J. Climate*, **17,** 3761–3774.
642 Ropelewski, C. F., and M. S. Halpert, 1987: Global and regional scale precipitation
643 patterns associated with the El Niño/ Southern Oscillation. *Mon. Wea. Rev.,* **115,**
644 1606–1626.
645 Schopf, P. S., and R. J. Burgman, 2006: A simple mechanism for ENSO residuals and
646 asymmetry. *J. Climate*, **19,** 3167–3179.
647 Su, J., R. Zhang, T. Li, X. Rong, J.-S. Kug, and C.-C. Hong, 2010: Causes of the El Niño
648 and La Niña amplitude asymmetry in the equatorial eastern Pacific, *J. Climate*, **23**,
649 605–617, doi:10.1175/2009JCLI2894.1.
650 Sun, D.-Z., and T. Zhang, 2006: A regulatory effect of ENSO on the time-mean thermal
651 stratification of the equatorial upper ocean. *Geophys. Res. Lett.*, **33,** L07710.
652 doi:10.1029/2005GL025296.

653 Sun, D.-Z., T. Zhang, C. Covey, S. Klein, W. Collins, J. Hack, J. Kiehl, G.A. Meehl, I.
654 Held, and M. Suarez, 2006: Radiative and Dynamical Feedbacks Over the Equatorial
655 Cold Tongue: Results from Nine Atmospheric GCMs. *J. Climate*, **19**, 4059-4074.
656 Sun, D.-Z., 2010: The Diabatic and Nonlinear Aspects of El Niño Southern Oscillation:
657 Implications for its Past and Future Behavior, in Climate Dynamics: Why Does
658 Climate Vary? (eds D.-Z. Sun and F. Bryan), American Geophysical Union,
659 Washington, D. C.. doi: 10.1029/2009GM000865.
660 Sun, D.-Z., 2003: A possible effect of an increase in the warm-pool SST on the
661 magnitude of El Niño warming, *J. Climate*, **16**, 185–205.
662 Sun, D.-Z., T. Zhang, and S.-I. Shin, 2004: The effect of subtropical cooling on the
663 amplitude of ENSO: A numerical study, *J. Climate*, **17**, 3786– 3798.
664 Sun, F., and J-Y. Yu, 2009: A 10–15-year modulation cycle of ENSO intensity. *J.*
665 *Climate*, **22,** 1718–1735.
666 Sun, Y., D.-Z. Sun, L. X. Wu, and F. Wang, 2013: Western Pacific Warm Pool and
667 ENSO Asymmetry in CMIP3 Models. *Adv. Atmos. Sci.*, **30**(3), 940–953, doi:
668 10.1007/s00376-012-2161-1.
669 Taylor, K. E., R. J. Stouffer, and G. A. Meehl, 2012: An overview of CMIP5 and the
670 experiment design, *Bull. Am. Meteorol. Soc.,* **93**, 485–498, doi:10.1175/BAMS-D-11-
671 00094.1.
672 van Oldenborgh, G. J., S. Philip, and M. Collins, 2005: El Niño in a changing climate: A
673 multi-model study. *Ocean Sci.,* **1,** 81–95.
674 Vialard, J., C. Menkes, J-P. Boulanger, P. Delecluse, E. Guilyardi, M. J. McPhaden, and
675 G. Madec, 2001: A model study of oceanic mechanisms affecting equatorial Pacific

676 sea surface temperature during the 1997–98 El Niño. *J. Phys. Oceanogr.*, **31,** 1649–
677 1675.
678 Watanabe, M., M. Chikira, Y. Imada, and M. Kimoto (2011), Convective control of
679 ENSO simulated in MIROC, *J. Climate*, **24**, 543–562, doi:10.1175/2010JCLI3878.1.
680 Xie, P., and P. A. Arkin, 1997: Global precipitation: A 17-year monthly analysis based on
681 gauge observations, satellite estimates, and numerical model outputs. *Bull. Amer.*
682 *Meteor. Soc.*, **78,** 2539–2558.
683 Zhang, G. J., and N. A. McFarlane, 1995: Sensitivity of climate simulations to the
684 parameterization of cumulus convection in the Canadian Climate Centre general
685 circulation model. *Atmos.–Ocean*, **33,** 407–446.
686 Zhang, T., D.-Z. Sun, R. Neale, and P. J. Rasch, 2009: An Evaluation of ENSO
687 Asymmetry in the Community Climate System Models: A View from the Subsurface.
688 *J. Climate*, **22**, 5933-5961.
689 Zhang, T., M. P. Hoerling, J. Perlwitz, D.-Z. Sun, and D. Murray, 2011: Physics of U.S.
690 surface temperature response to ENSO. *J. Climate*, **24**, 4874–4887.
691 Zhang, X., and M. J. McPhaden, 2006: Wind stress variations and interannual sea surface
692 temperature anomalies in the eastern equatorial Pacific. *J. Climate*, **19**, 226–241.
693 Zhu, J., Z. Sun, and G. Zhou, 2007: A note on the role of meridional wind stress
694 anomalies and heat flux in ENSO simulations. *Adv. Atmos. Sci.*, **24**(4), 729–738, doi:
695 10.1007/s00376-007-0729-y.
696

## Table and Figure Captions

Table 1: Standard deviation and skewness of the interannual variability in Niño-3 SST from four forced ocean model experiments. The mean as well as the anomaly part of the surface winds used in these experiments are listed. The length of observed wind data used in the forced runs is 30-year for SODA wind stress (1979–2008). The length of simulated wind data used is 27-year for CAM4 (1979-2005) and 30-year for other models (1979-2008).

Figure 1: Standard deviation (upper) and skewness (bottom) of the interannual variability in Niño-3 SST from observations and CMIP5 coupled models. The length of data used in the calculation is 50 years for all the models and observations (1950-99).

Figure 2: The sum of the composite SST anomalies between the two phases of ENSO from observations and CMIP5 coupled models. Following the study of Zhang et al. (2009), the positive (negative) anomalies of Niño-3 SST with a value greater than 0.5°C (−0.5°C) are selected to construct composites of warm (cold) events. Same data used as for Figure 1.

Figure 3: The sum of the composite equatorial ($5^oS$-$5^oN$) upper ocean temperature anomalies between the two phases of ENSO from observations and CMIP5 coupled models. The length of data used in the calculation is 50 years for all the models and SODA data (1950-1999).

720 Figure 4: Composite SST anomalies for the warm phase of ENSO from observations and
721 coupled models.
722
723 Figure 5: Composite anomalies of equatorial ($5^{o}$S-$5^{o}$N) upper ocean temperature for the
724 warm phase of ENSO from observations and coupled models.
725
726 Figure 6: Probability distribution function (PDF) of monthly-mean Niño-3 SST
727 anomalies from observations and CMIP5 coupled models. The ensemble mean of the
728 results from fourteen coupled models is also included in the figure. A bin width of 0.2°C
729 is used in the calculation. Same data used as for Figure 1.
730
731 Figure 7: The sum of the composite anomalies for the two phases of ENSO for
732 precipitation (shaded) and zonal wind stress (contours) from observations and CMIP5
733 coupled models. The length of data used in the calculation is 50 years for all the models,
734 30 years for CMAP precipitation (1979–2008), and 50 years for SODA zonal wind stress
735 (1959–2008).
736
737 Figure 8: The sum of the composite precipitation anomalies between the two phases of
738 ENSO from observations and the corresponding AMIP runs of CMIP5 coupled models.
739 The length of data used in the calculation is 30 years for CMAP precipitation (1979–
740 2008), 27 years for CAM4 (1979-2005) and 30 years for the other models (1979-2008).
741

742 Figure 9: The sum of the composite precipitation anomalies of the two phases of ENSO
743 averaged over the eastern Pacific (120°W-70°W, 10°S-10°N) from CMIP5 coupled
744 models (top panel) and the corresponding AMIP runs (bottom panel). The corresponding
745 observational value is also included in the figures. The length of data used in the
746 calculation is 30 years for CMAP precipitation (1979–2008), and 50 years for all the
747 coupled models. The length of data used for AMIP runs is the same as for Figure 8.
748
749 Figure 10: Composite precipitation anomalies for the warm phase of ENSO averaged
750 over the eastern Pacific (120°W-70°W, 10°S-10°N) from CMIP5 coupled models (top
751 panel) and the corresponding AMIP runs (bottom panel).
752
753 Figure 11: The warm phase precipitation anomalies (left panel) and zonal wind stress
754 anomalies (right panel) from observations, the ensemble mean of the model results, and
755 their differences. Green lines indicate the positions that the equatorial westerly wind
756 anomaly can reach. Fourteen CMIP5 AMIP runs during the warm phase are used in
757 calculating the ensemble mean. The length of observational data used in the calculation is
758 30 years for CMAP precipitation and SODA zonal wind stress (1979–2008). The length
759 of data used for AMIP runs is the same as for Figure 8.
760
761 Figure 12: The time-mean zonal wind stress (top) over the equatorial central and eastern
762 Pacific (170°E-70°W, 5°S-5°N) and the skewness of the interannual anomalies of the
763 zonal wind stress (bottom) over the central Pacific (160°E-140°W, 10°S-5°N) from
764 observations and CMIP5 AMIP runs. The ensemble mean of the results from fourteen

765 AMIP runs is also included in the figure. Monthly anomalies are used to calculate the
766 skewness. The length of observational data used in the calculation is 30 years for SODA
767 zonal wind stress (1979–2008). The length of data used for AMIP runs is the same as for
768 Figure 8.
769
770 Figure 13: The difference between observations and the ensemble mean zonal wind stress
771 annual climatology (top) and the difference between observations and ensemble mean
772 precipitation annual climatology (bottom) from fourteen CMIP5 AMIP runs. The length
773 of observational data used in the calculation is 30 years for CMAP precipitation and
774 SODA zonal wind stress (1979–2008). The length of data used for AMIP runs is the same
775 as for Figure 8.
776
777 Figure 14: Probability distribution function (PDF) of monthly-mean Niño-3 SST
778 anomalies from four forced ocean experiments as listed in Table 1. A bin width of 0.2°C
779 is used in the calculation. The length of data used is 30 years (1979-2008).
780
781 Figure 15: The sum of the composite anomalies of the two phases of ENSO for SST (left
782 panel) and the equatorial ($5^{o}$S-$5^{o}$N) upper ocean temperature (right panel) in the four
783 forced ocean experiments as listed in Table 1.
784
785 Figure 16: Composite anomalies of SST (left panel) and the equatorial ($5^{o}$S-$5^{o}$N) upper
786 ocean temperature (right panel) for the warm phase of ENSO in the four forced ocean
787 experiments as listed in Table 1.

788

789 Figure 17: Composite anomalies of SST (left panel) and the equatorial ($5^oS$-$5^oN$) upper
790 ocean temperature (right panel) for the cold phase of ENSO in the four forced ocean
791 experiments as listed in Table 1.

792

793 Figure 18: Time mean SST difference (left panel) and the equatorial ($5^oS$-$5^oN$) upper
794 ocean temperature difference (right panel) of Experiment II, Experiment III, and
795 Experiment IV from Experiment I.

796

Table 1: Standard deviation and skewness of the interannual variability in Niño-3 SST from four forced ocean model experiments. The mean as well as the anomaly part of the surface winds used in these experiments are listed. The length of observed wind data used in the forced runs is 30 years for SODA wind stress (1979–2008). The length of simulated wind data used is 27 years for CAM4 (1979-2005) and 30 years for other models (1979-2008).

| Experiment ID (label in figures) | Surface wind stress | | Statistics of Nino3 SSTA | |
|---|---|---|---|---|
| | Climatology | Anomaly | Skewness | Standard deviation( $^0$C) |
| Experiment I | Observation | Observation | 1.16 | 0.75 |
| | | | | |
| Experiment II | CMIP5 amip ensemble | Observation | 0.92 | 0.73 |
| | | | | |
| Experiment III | CMIP5 amip ensemble | CMIP5 amip ensemble | 0.70 | 0.63 |
| | | | | |
| Experiment IV | Observation | CMIP5 amip ensemble | 1.18 | 0.64 |

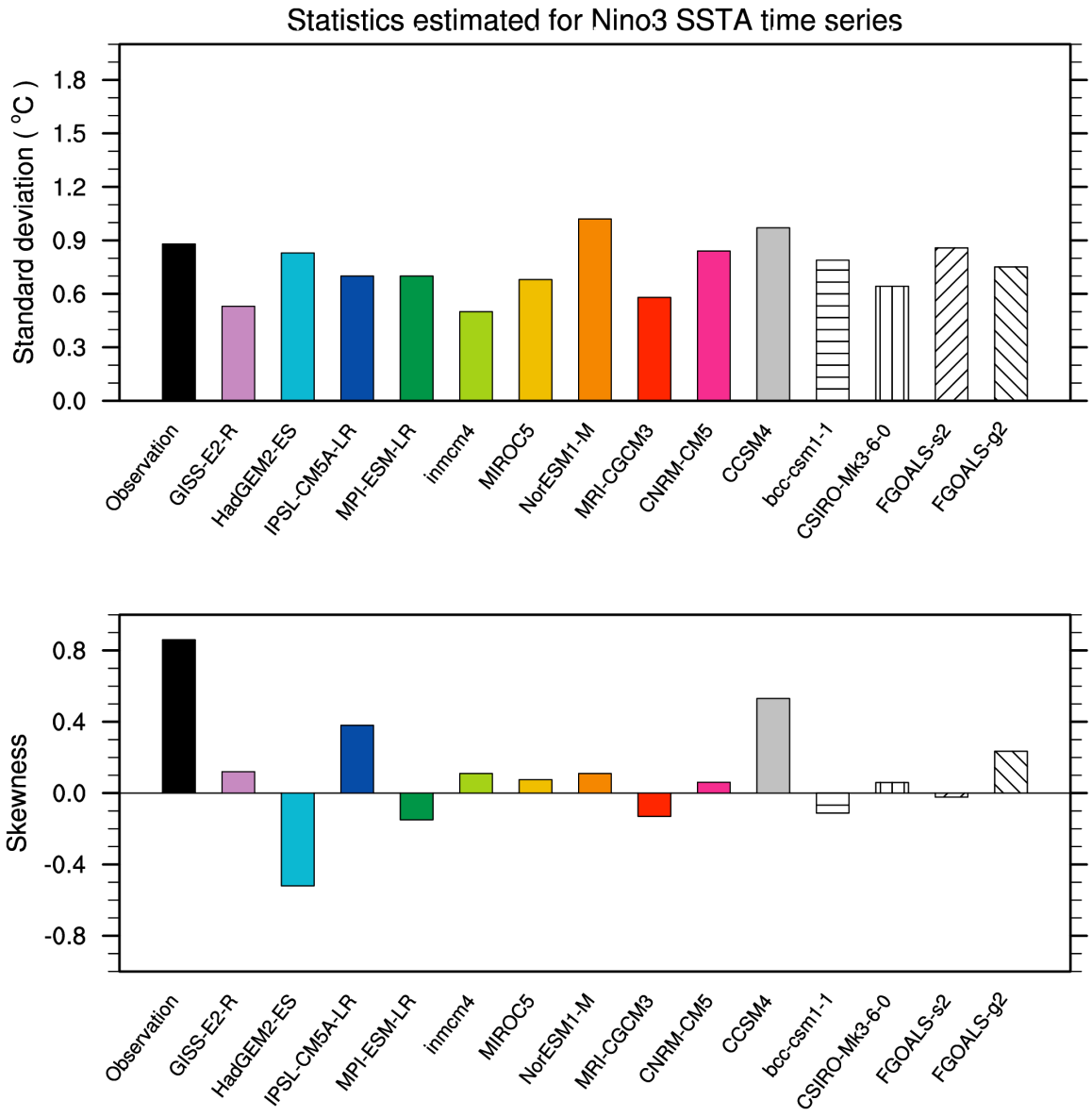


Figure 1: Standard deviation (upper) and skewness (bottom) of the interannual variability in Niño-3 SST from observations and CMIP5 coupled models. The length of data used in the calculation is 50 years for all the models and observations (1950-99).

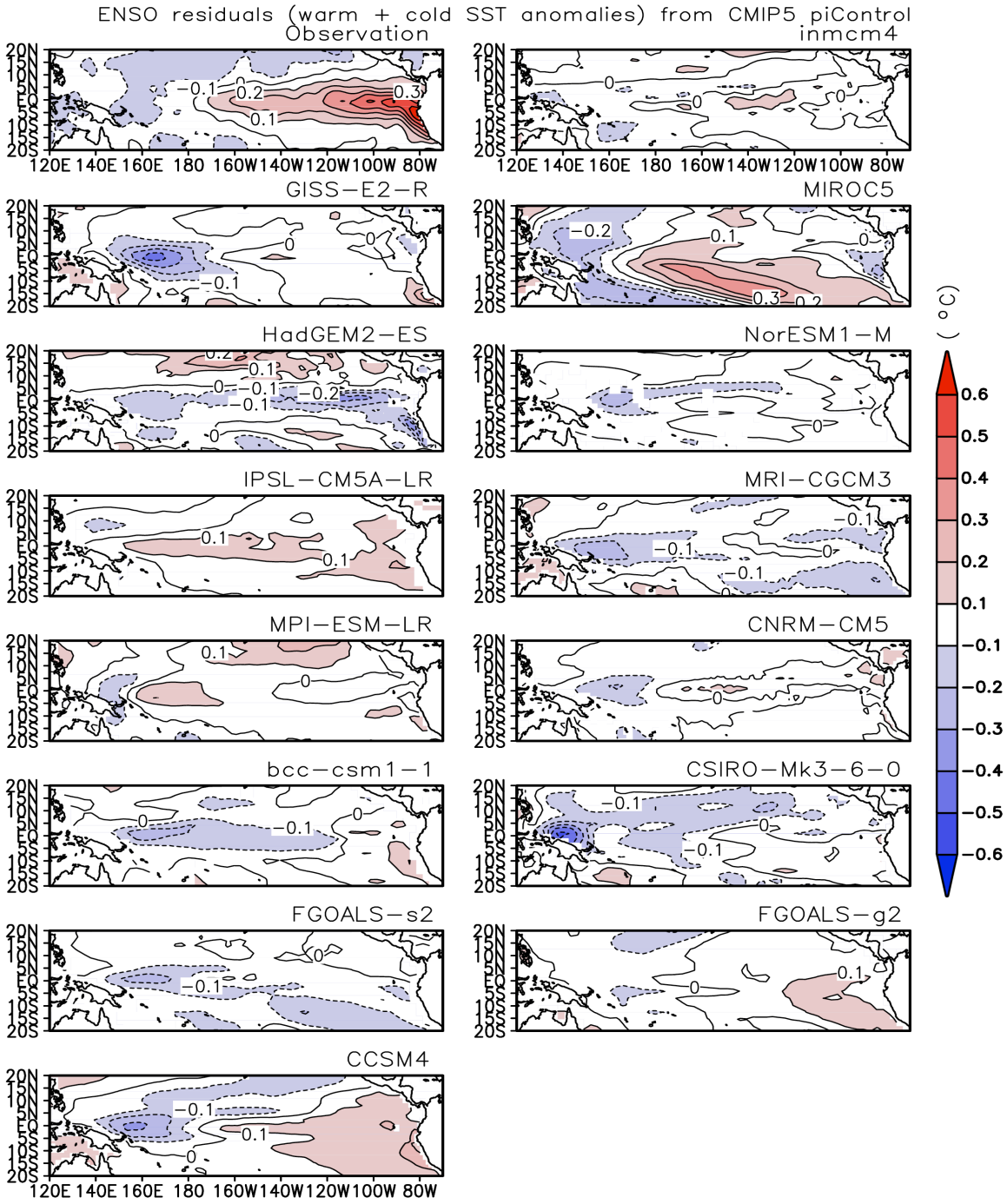


Figure 2: The sum of the composite SST anomalies between the two phases of ENSO from observations and CMIP5 coupled models. Following the study of Zhang et al. (2009), the positive (negative) anomalies of Niño-3 SST with a value greater than 0.5°C (−0.5°C) are selected to construct composites of warm (cold) events. Same data used as for Figure 1.

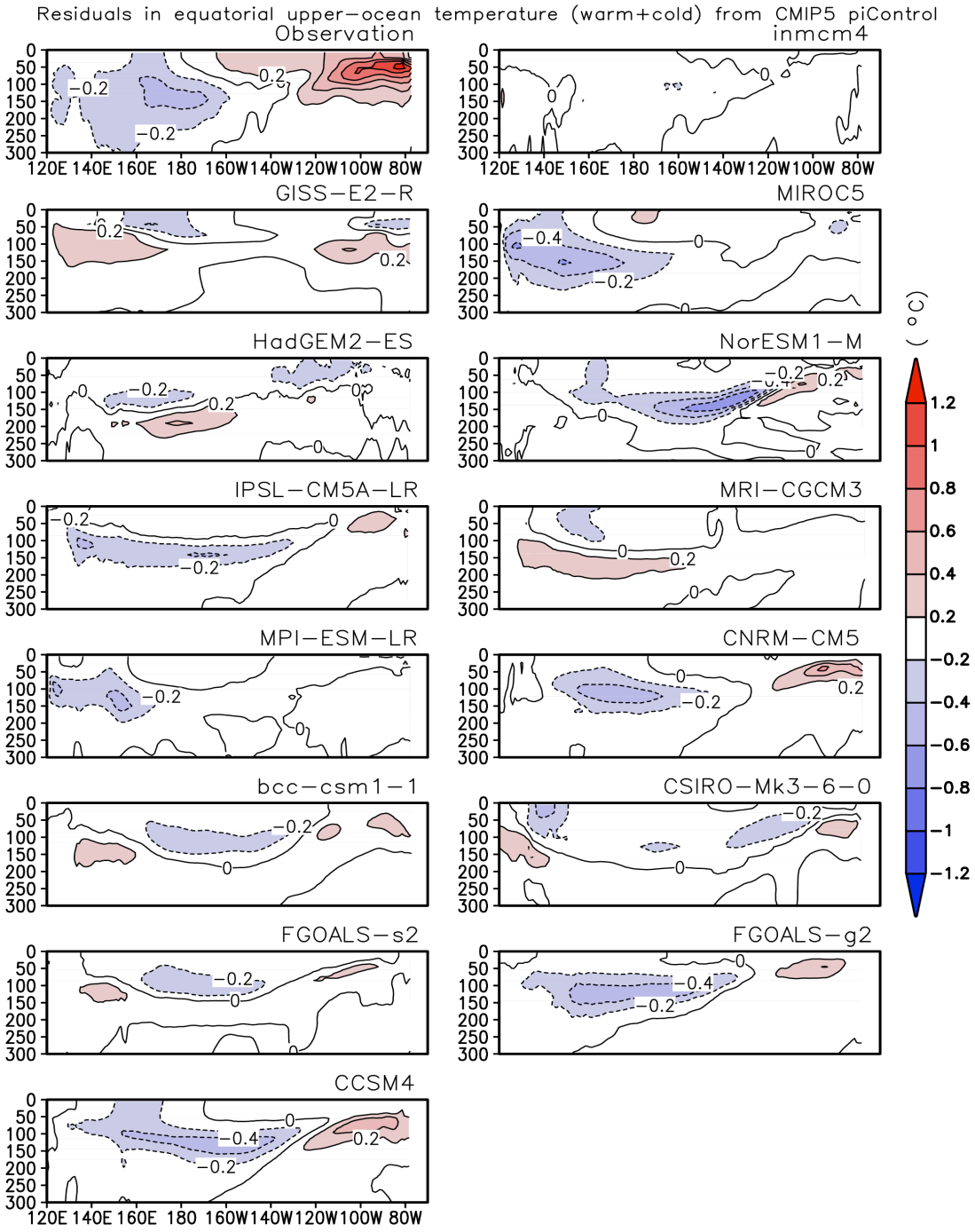


Figure 3: The sum of the composite equatorial (5°S-5°N) upper ocean temperature anomalies between the two phases of ENSO from observations and CMIP5 coupled models. The length of data used in the calculation is 50 years for all the models and SODA data (1950-1999).

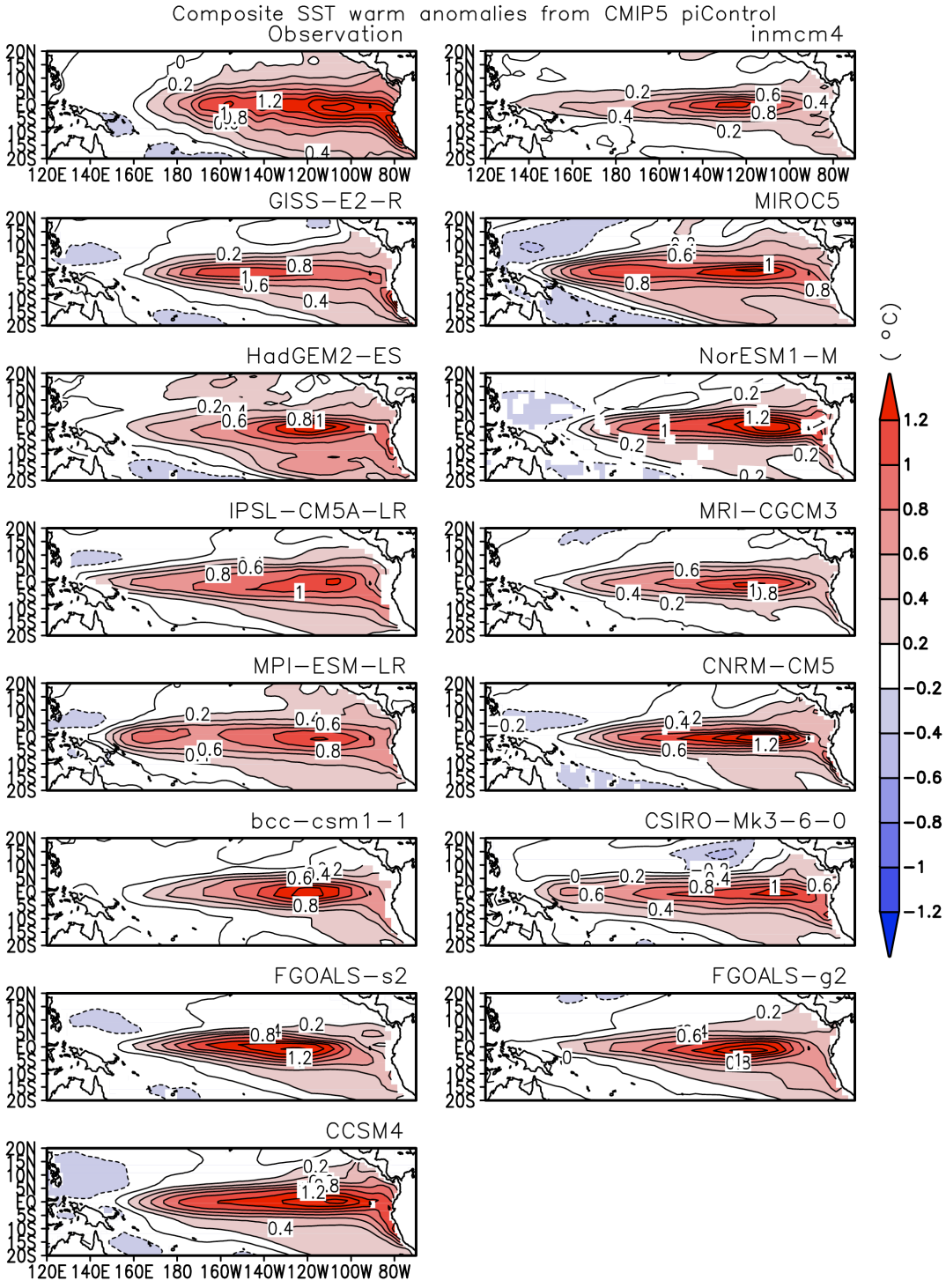


Figure 4: Composite SST anomalies for the warm phase of ENSO from observations and coupled models.

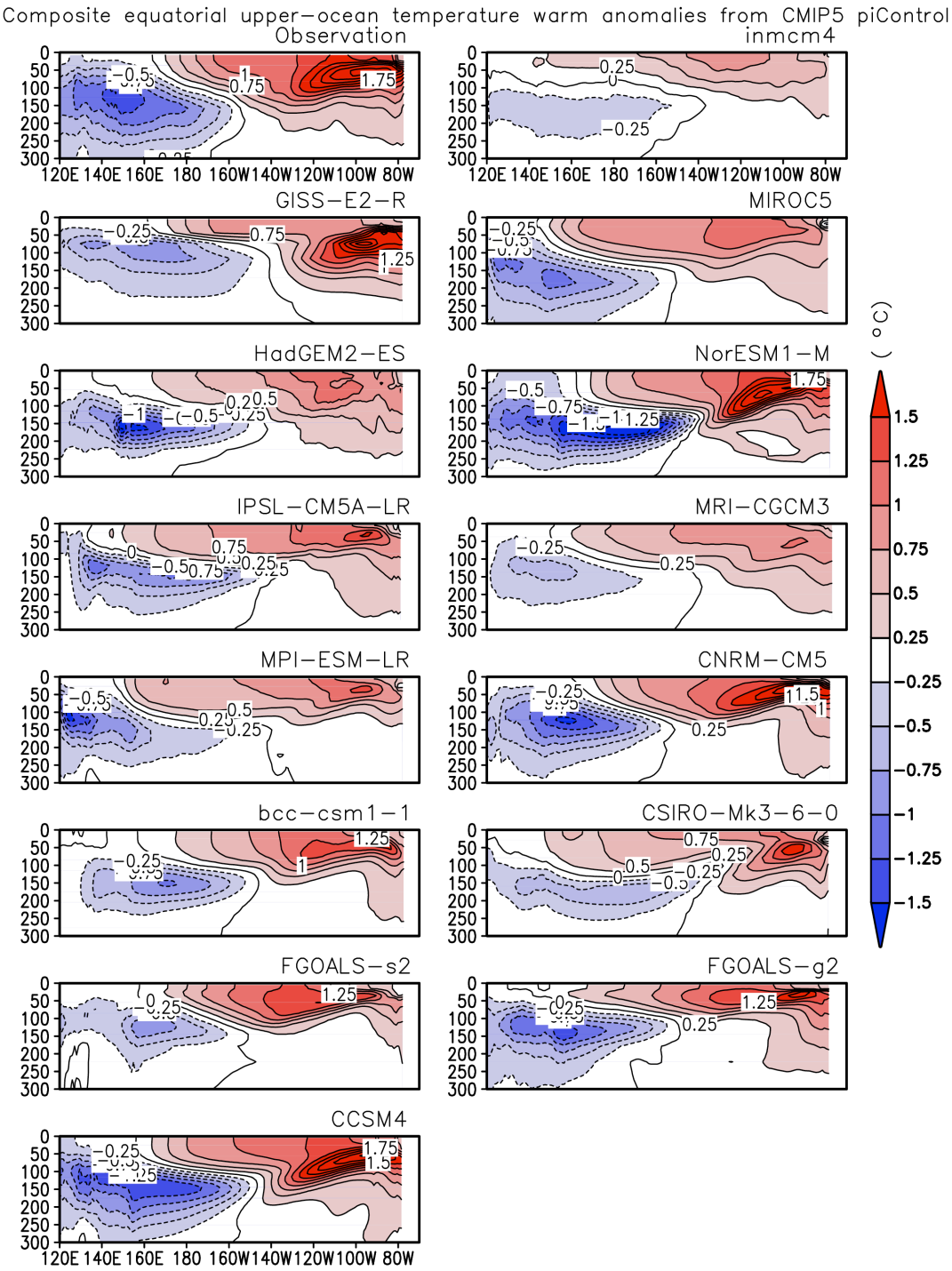


Figure 5: Composite anomalies of equatorial (5°S-5°N) upper ocean temperature for the warm phase of ENSO from observations and coupled models.

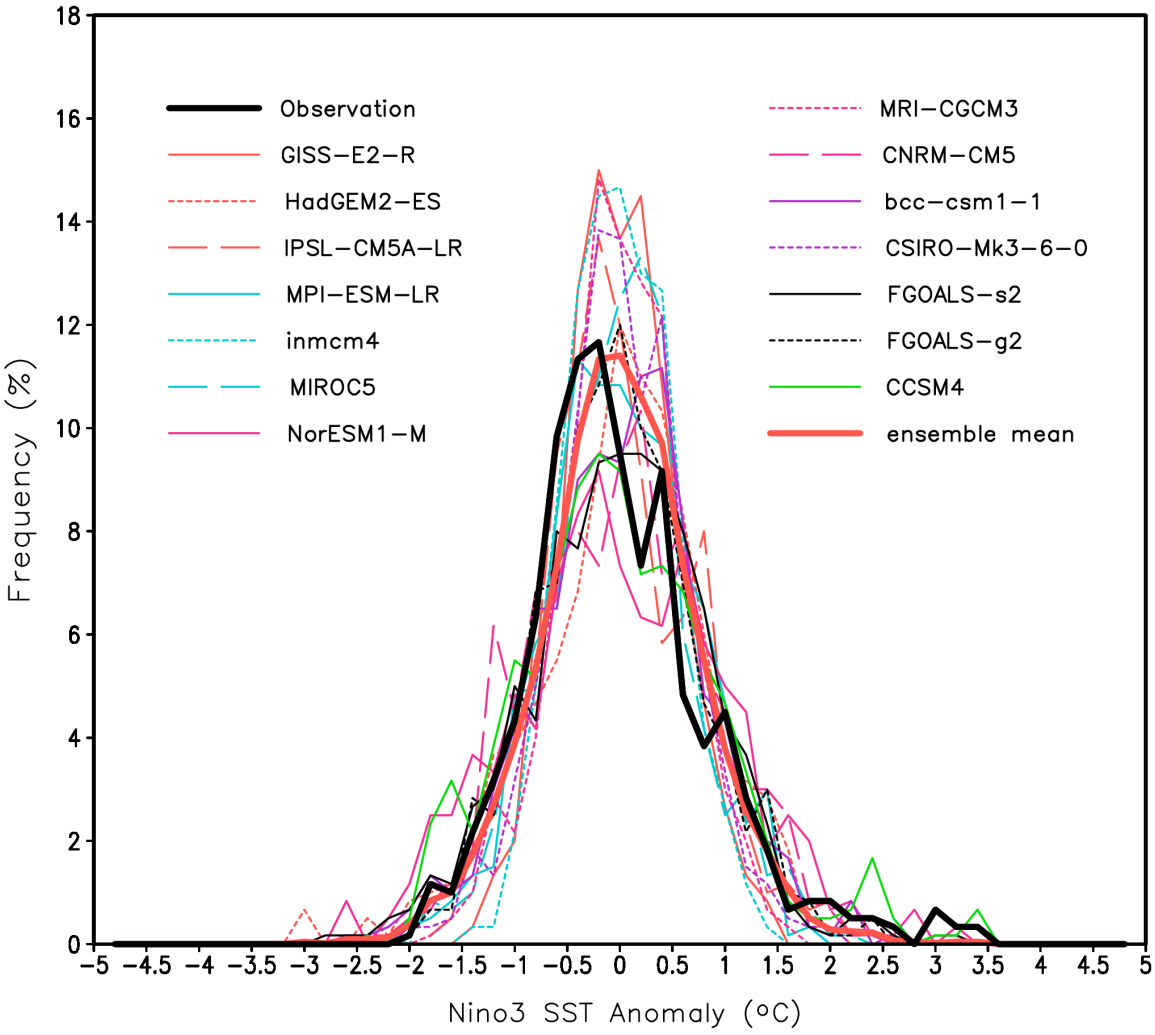


Figure 6: Probability distribution function (PDF) of monthly-mean Niño-3 SST anomalies from observations and CMIP5 coupled models. The ensemble mean of the results from fourteen coupled models is also included in the figure. A bin width of 0.2°C is used in the calculation. Same data used as for Figure 1.

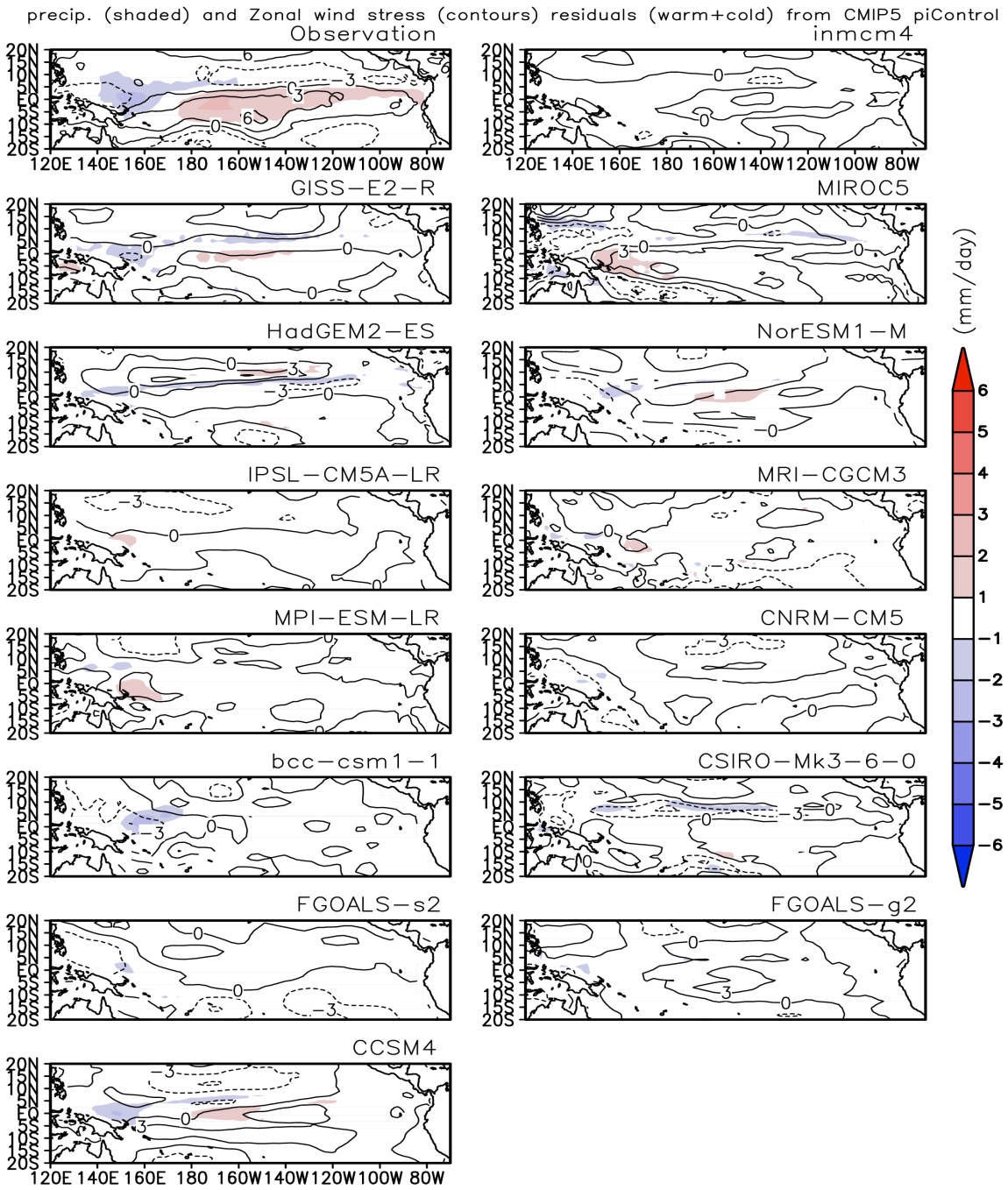


Figure 7: The sum of the composite anomalies for the two phases of ENSO for precipitation (shaded) and zonal wind stress (contours) from observations and CMIP5 coupled models. The length of data used in the calculation is 50 years for all the models, 30 years for CMAP precipitation (1979–2008), and 50 years for SODA zonal wind stress (1959–2008).

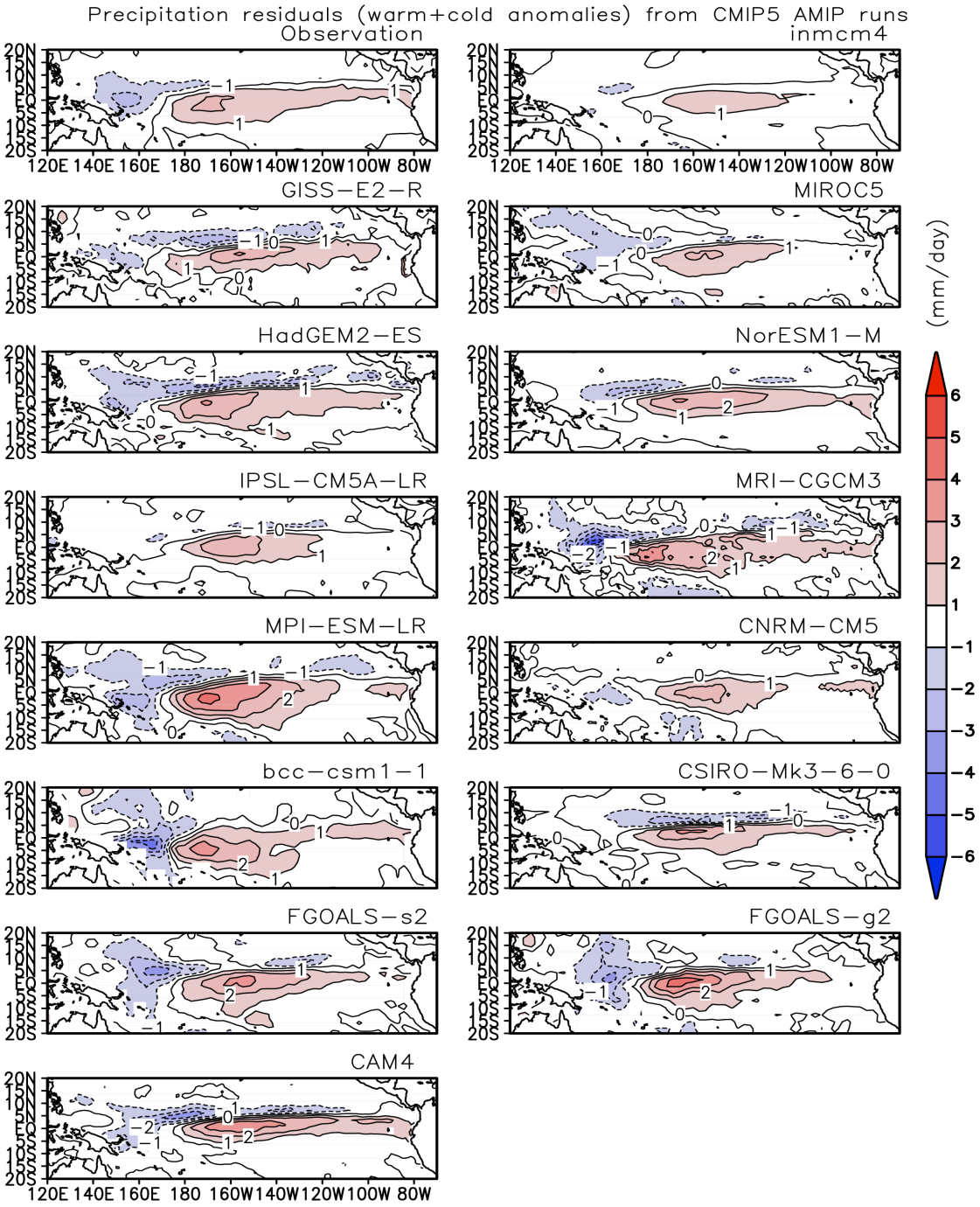


Figure 8: The sum of the composite precipitation anomalies between the two phases of ENSO from observations and the corresponding AMIP runs of CMIP5 coupled models. The length of data used in the calculation is 30 years for CMAP precipitation (1979–2008), 27 years for CAM4 (1979-2005) and 30 years for the other models (1979-2008).

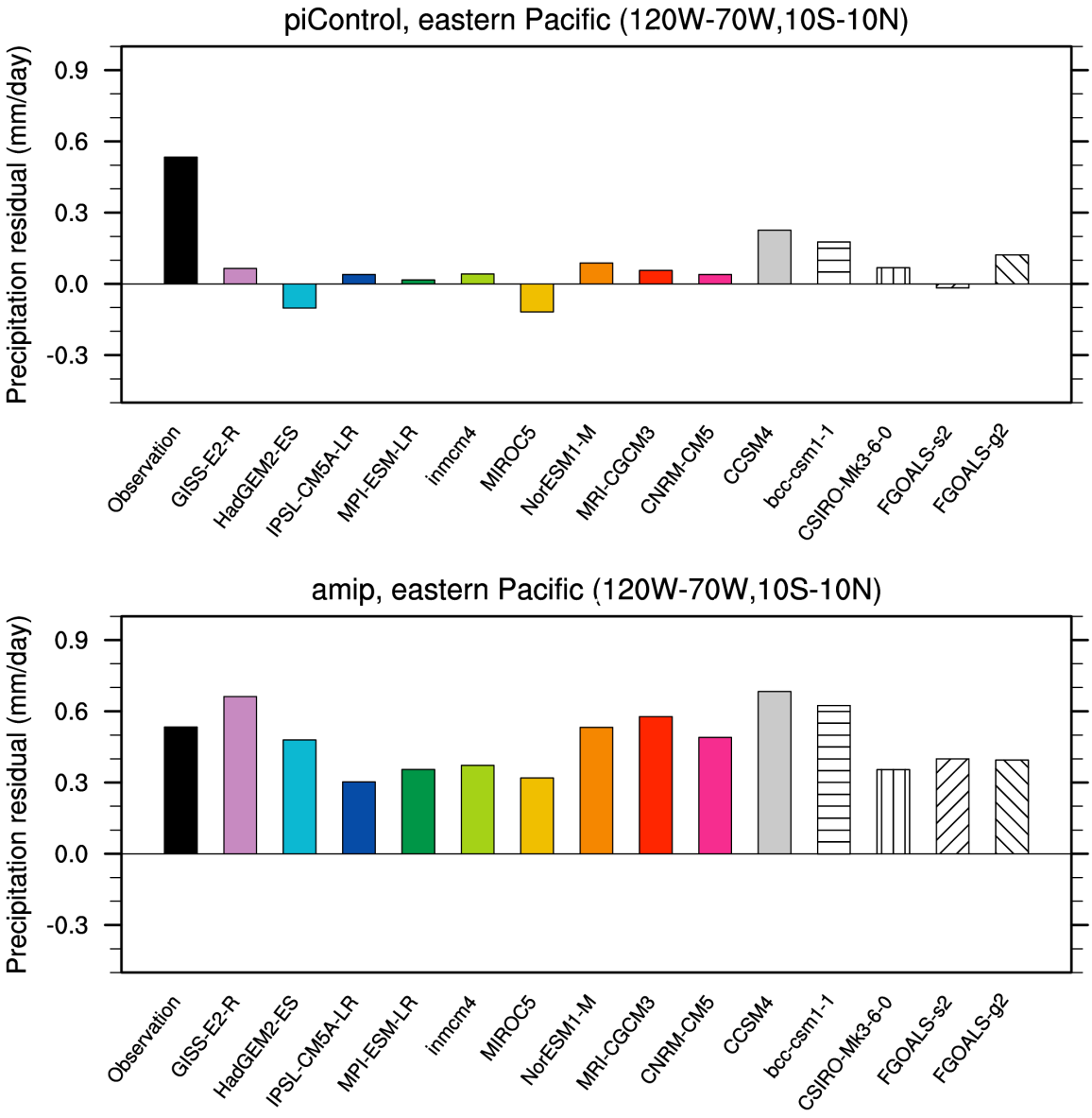


Figure 9: The sum of the composite precipitation anomalies of the two phases of ENSO averaged over the eastern Pacific (120°W-70°W, 10°S-10°N) from CMIP5 coupled models (top panel) and the corresponding AMIP runs (bottom panel). The corresponding observational value is also included in the figures. The length of data used in the calculation is 30 years for CMAP precipitation (1979–2008), and 50 years for all the coupled models. The length of data used for AMIP runs is the same as for Figure 8.

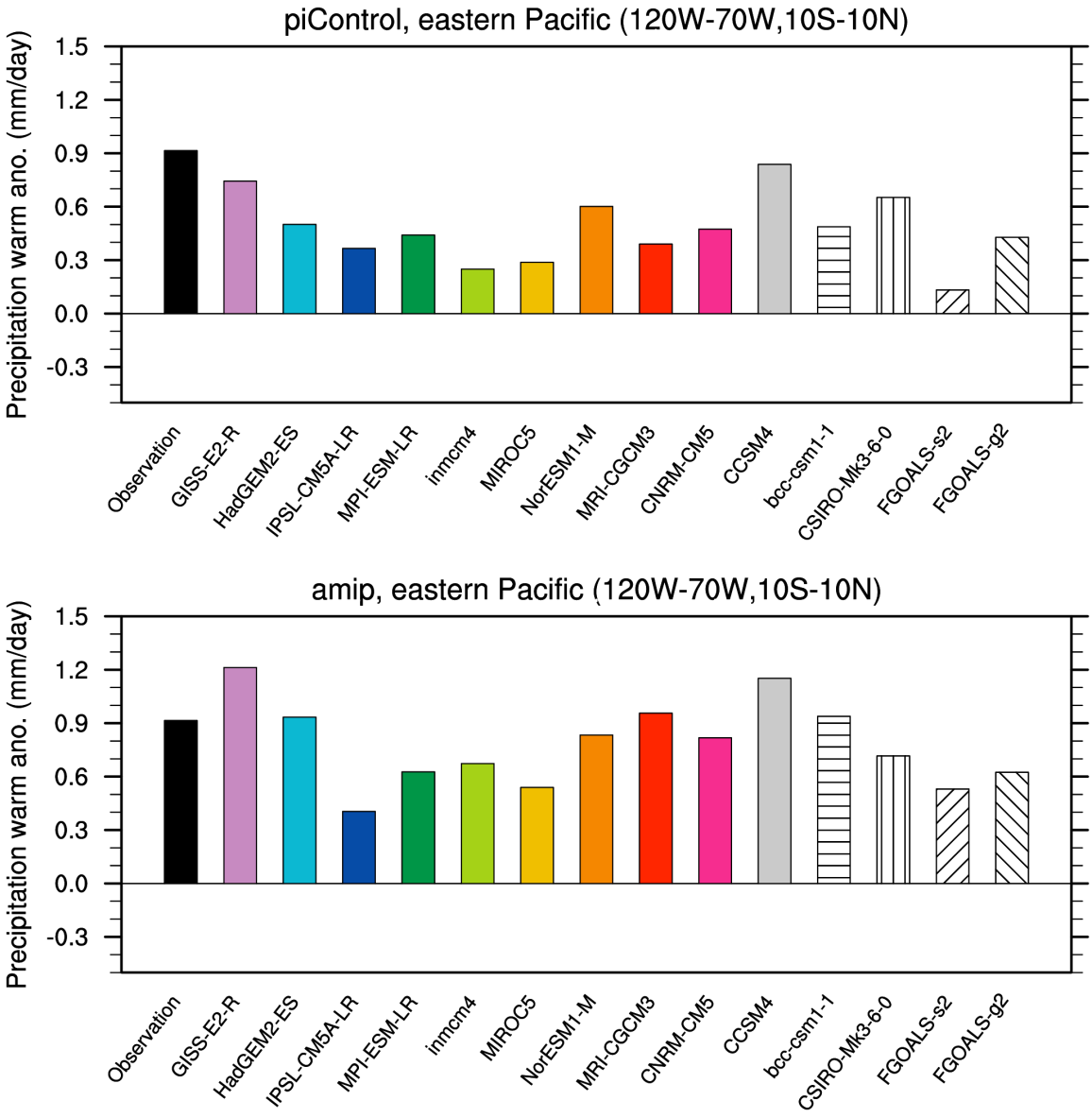


Figure 10: Composite precipitation anomalies for the warm phase of ENSO averaged over the eastern Pacific (120°W-70°W, 10°S-10°N) from CMIP5 coupled models (top panel) and the corresponding AMIP runs (bottom panel).

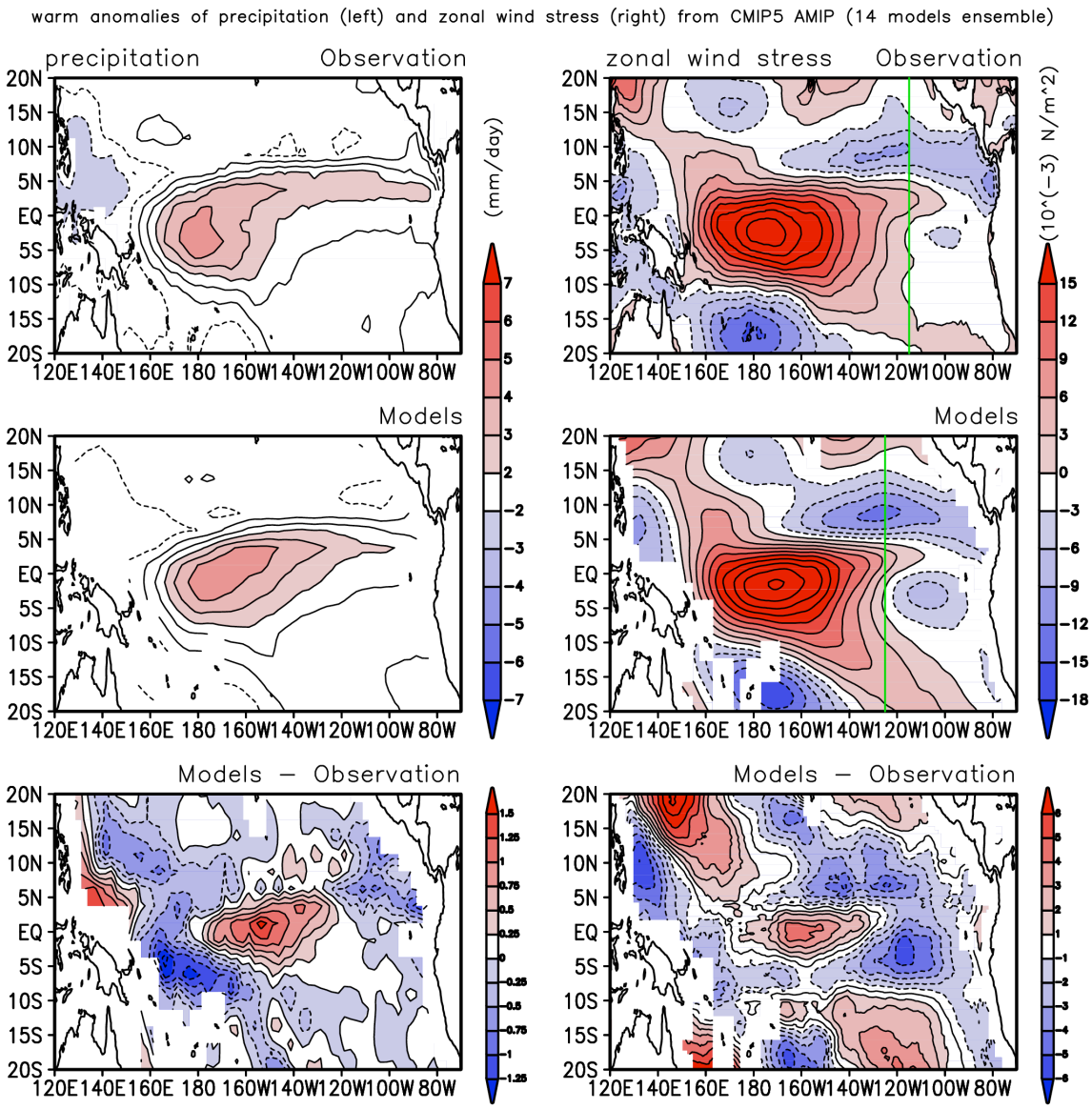


Figure 11: The warm phase precipitation anomalies (left panel) and zonal wind stress anomalies (right panel) from observations, the ensemble mean of the model results, and their differences. Green lines indicate the positions that the equatorial westerly wind anomaly can reach. Fourteen CMIP5 AMIP runs during the warm phase are used in calculating the ensemble mean. The length of observational data used in the calculation is 30 years for CMAP precipitation and SODA zonal wind stress (1979–2008). The length of data used for AMIP runs is the same as for Figure 8.

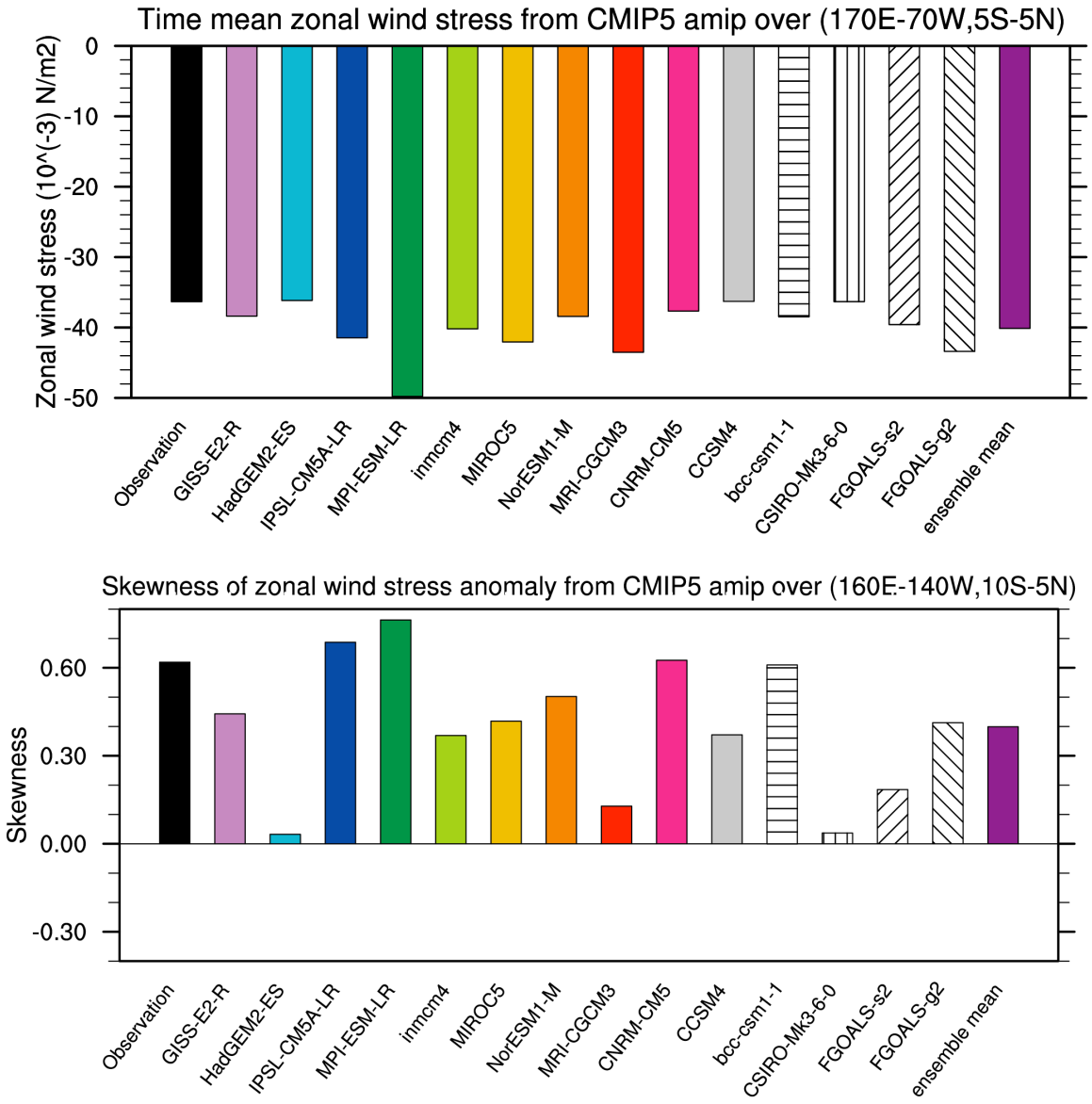


Figure 12: The time-mean zonal wind stress (top) over the equatorial central and eastern Pacific (170°E-70°W, 5°S-5°N) and the skewness of the interannual anomalies of the zonal wind stress (bottom) over the central Pacific (160°E-140°W, 10°S-5°N) from observations and CMIP5 AMIP runs. The ensemble mean of the results from fourteen AMIP runs is also included in the figure. Monthly anomalies are used to calculate the skewness. The length of observational data used in the calculation is 30 years for SODA zonal wind stress (1979–2008). The length of data used for AMIP runs is the same as for Figure 8.

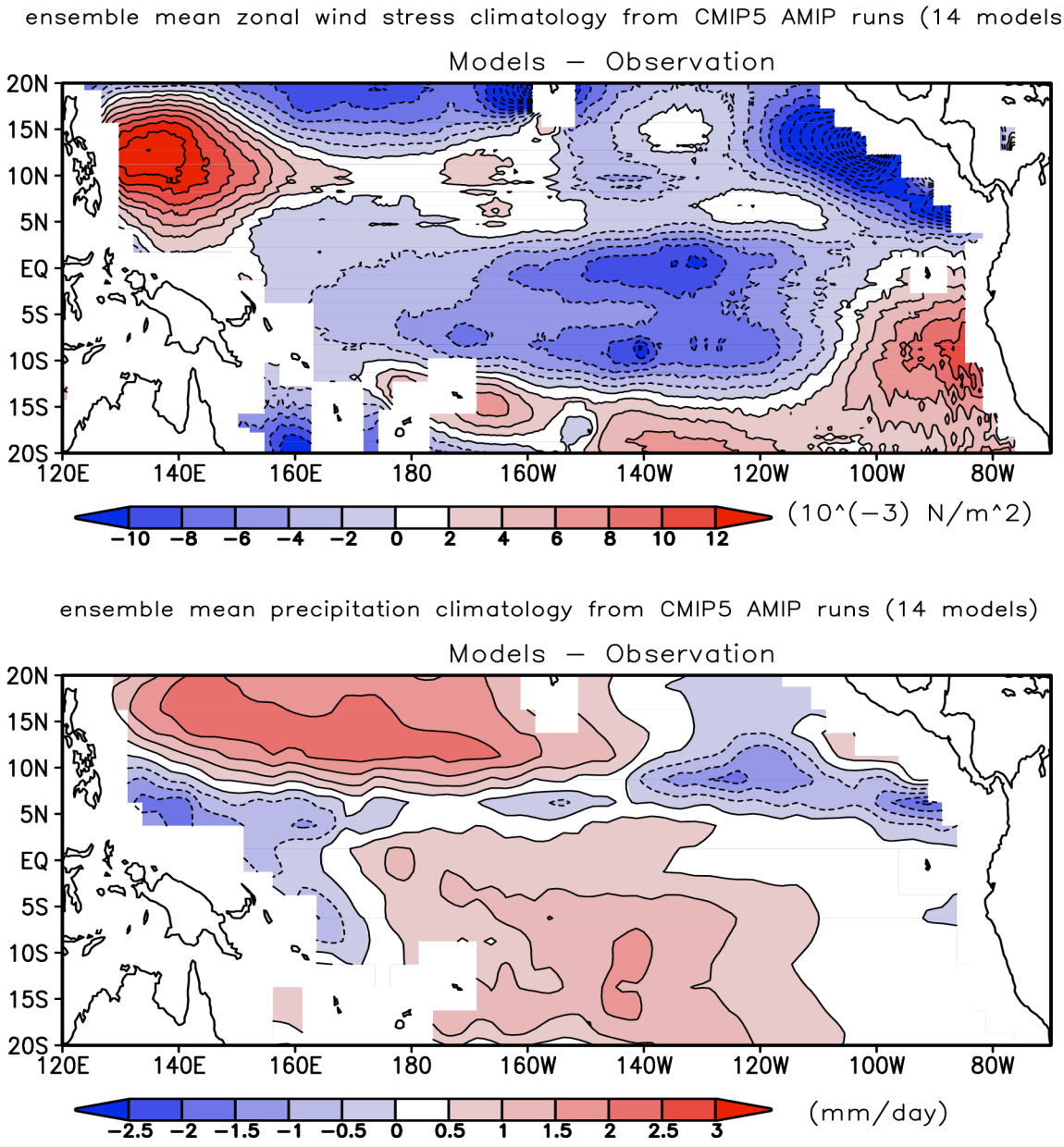


Figure 13: The difference between observations and the ensemble mean zonal wind stress annual climatology (top) and the difference between observations and ensemble mean precipitation annual climatology (bottom) from fourteen CMIP5 AMIP runs. The length of observational data used in the calculation is 30 years for CMAP precipitation and SODA zonal wind stress (1979–2008). The length of data used for AMIP runs is the same as for Figure 8.

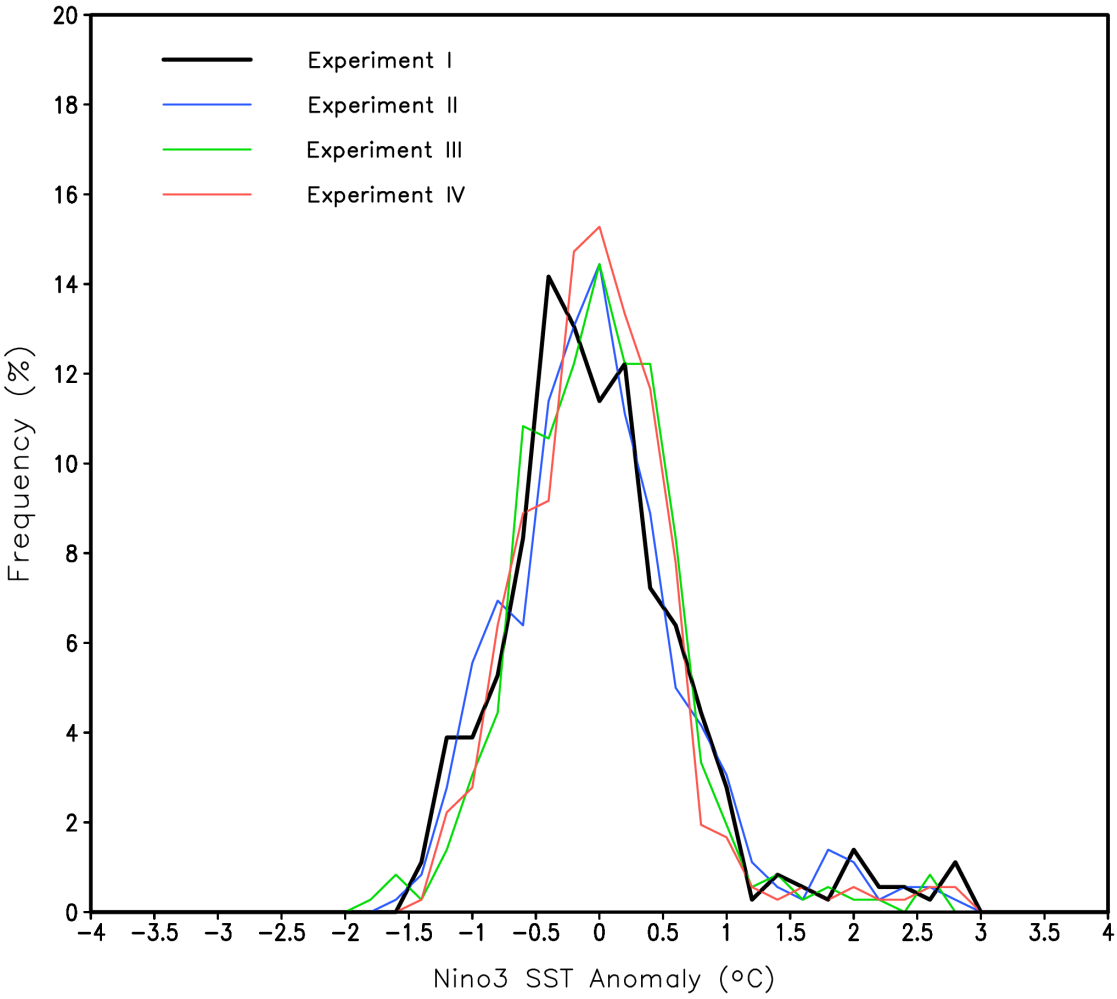


Figure 14: Probability distribution function (PDF) of monthly-mean Niño-3 SST anomalies from four forced ocean experiments as listed in Table 1. A bin width of 0.2°C is used in the calculation. The length of data used is 30 years (1979-2008).

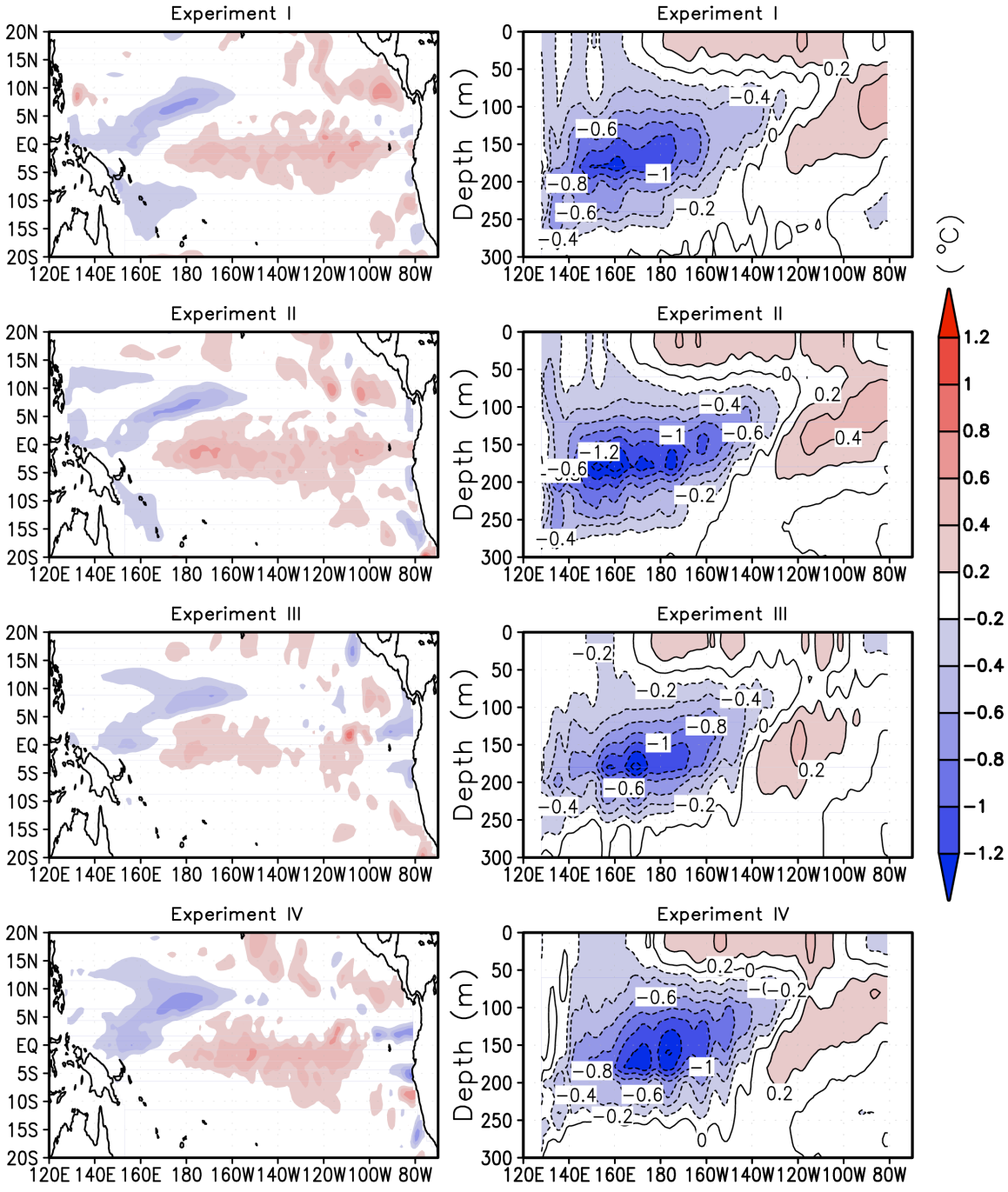


Figure 15: The sum of the composite anomalies of the two phases of ENSO for SST (left panel) and the equatorial (5°S-5°N) upper ocean temperature (right panel) in the four forced ocean experiments as listed in Table 1.

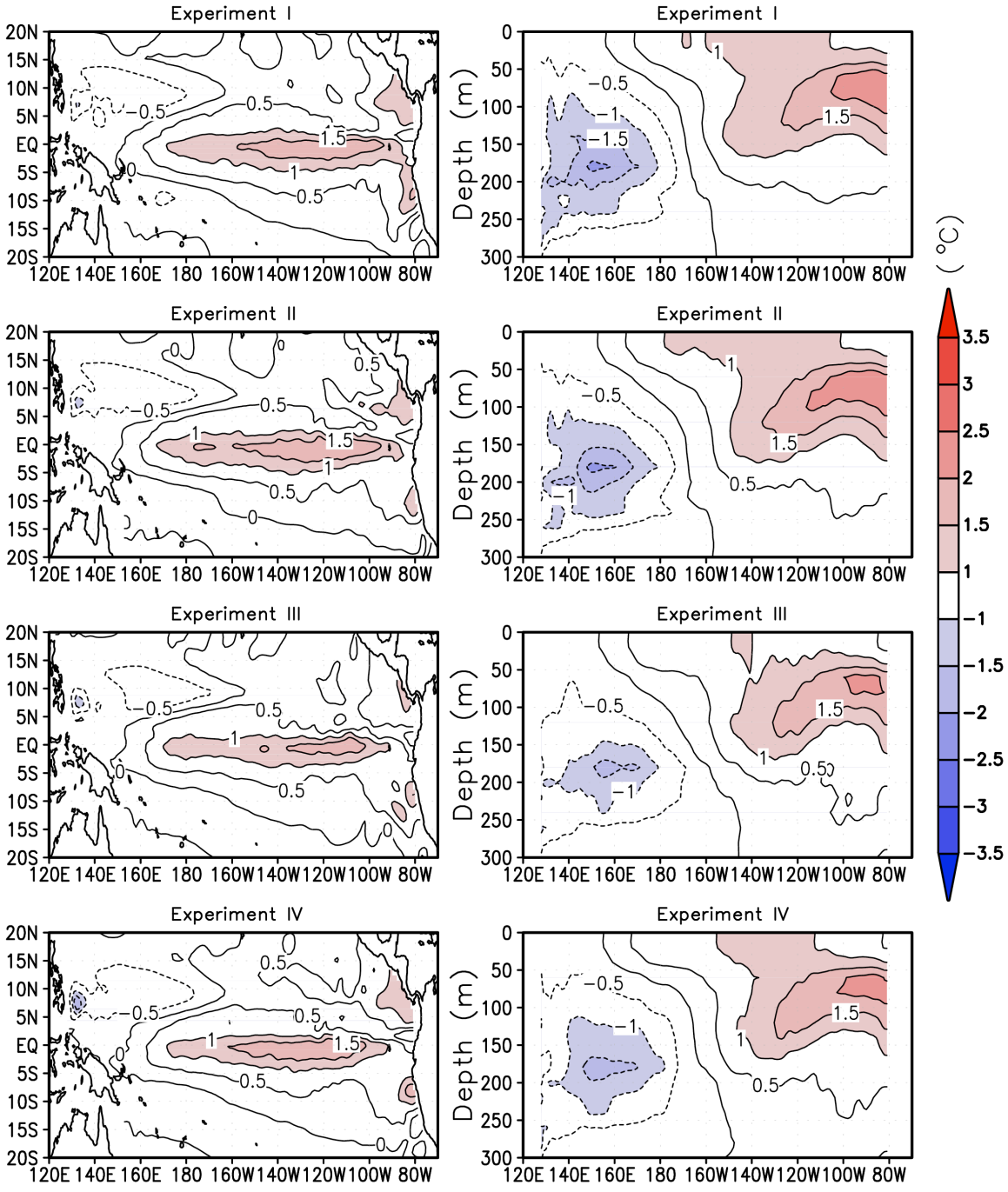


Figure 16: Composite anomalies of SST (left panel) and the equatorial (5°S-5°N) upper ocean temperature (right panel) for the warm phase of ENSO in the four forced ocean experiments as listed in Table 1.

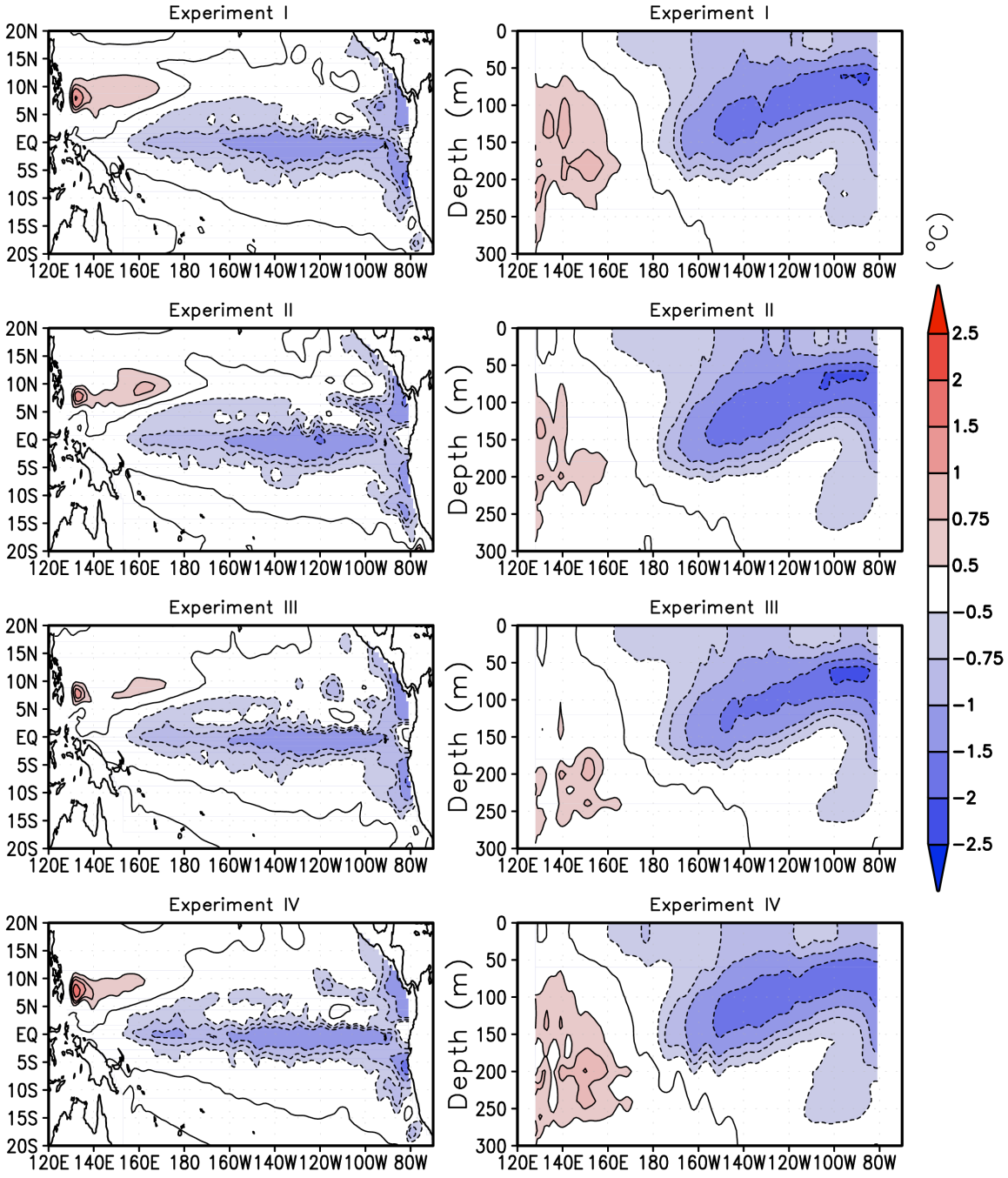


Figure 17: Composite anomalies of SST (left panel) and the equatorial ($5^{o}$S-$5^{o}$N) upper ocean temperature (right panel) for the cold phase of ENSO in the four forced ocean experiments as listed in Table 1.

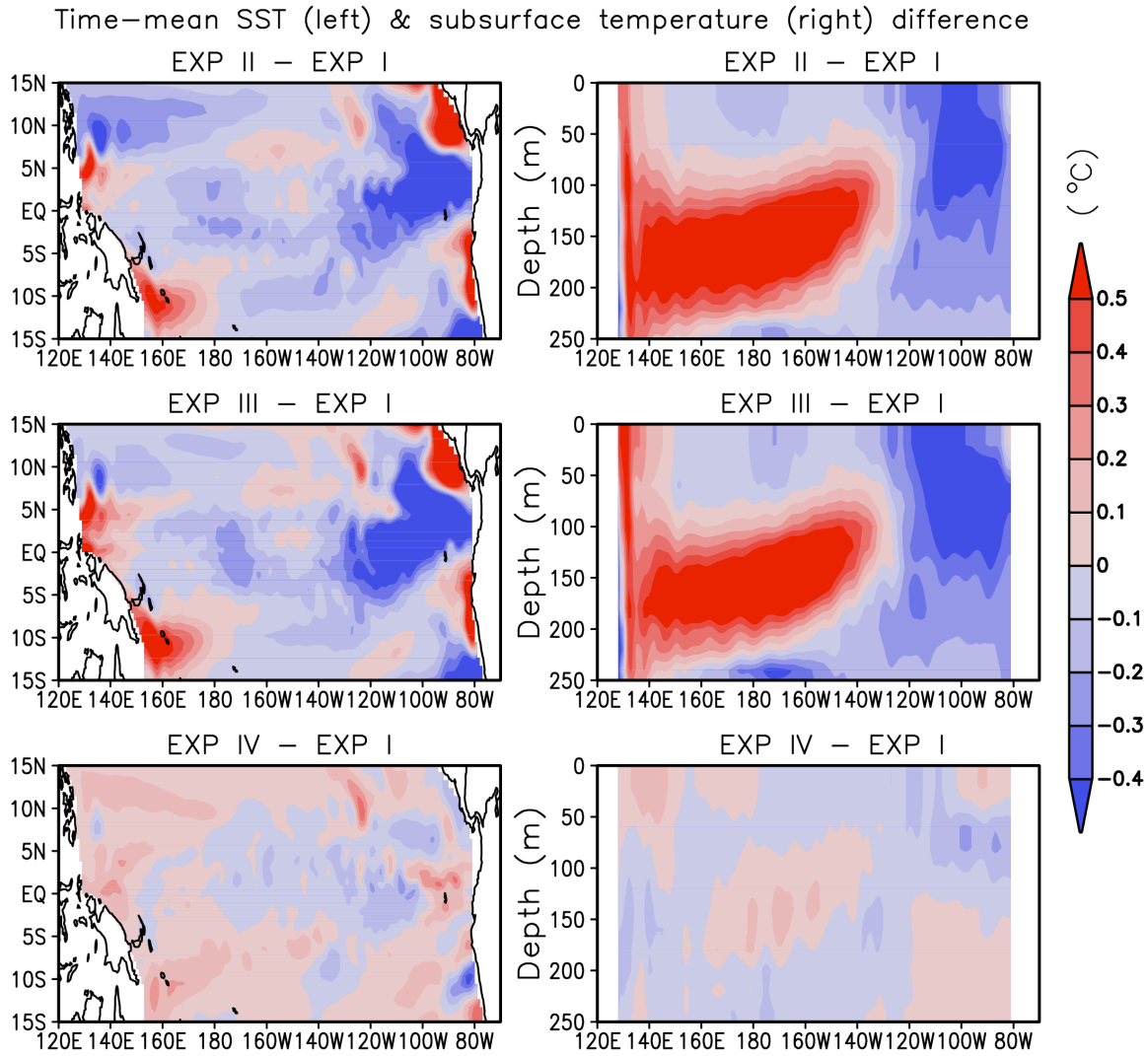


Figure 18: Time mean SST difference (left panel) and the equatorial ($5^{o}$S-$5^{o}$N) upper ocean temperature difference (right panel) of Experiment II, Experiment III, and Experiment IV from Experiment I.